Anthropogenic and natural controls on atmospheric δ^{13}C-CO$_2$ variations in the Yangtze River Delta: Insights from a carbon isotope modeling framework

Cheng Hu[1, 2*], Jiaping Xu[3], Cheng Liu[4], Yan Chen[3], Dong Yang[5], Wenjing Huang[2], Lichen Deng[6], Shoudong Liu[2], Timothy J. Griffis[7**], and Xuhui Lee [8]

[1] College of Biology and the Environment, Joint Center for sustainable Forestry in Southern China, Nanjing Forestry University, Nanjing, 210037, China

[2] Yale-NUIST Center on Atmospheric Environment, International Joint Laboratory on Climate and Environment Change (ILCEC), Nanjing University of Information, Science & Technology, Nanjing, 210044, China

[3] Jiangsu Climate Center, China Meteorological Administration, Nanjing, 210009, China

[4] Jiangxi Province Key Laboratory of the Causes and Control of Atmospheric Pollution, East China University of Technology, Nanchang, 330013, China

[5] Ningbo Meteorological Observatory, Ningbo, 315012, China

[6] Ecological Meteorology Center, Jiangxi Meteorological Bureau, Nanchang, 330096, China

[7] Department of Soil, Water, and Climate, University of Minnesota-Twin Cities, St. Paul, Minnesota, USA

[8] School of Forestry and Environmental Studies, Yale University, New Haven, Connecticut, USA

Correspondence:

*Cheng Hu, College of Biology and the Environment, Joint Center for sustainable Forestry in Southern China, Nanjing Forestry University, Nanjing, 210037, China. nihaohucheng@163.com or huxxx991@umn.edu

** Timothy J. Griffis, Department of Soil, Water, and Climate, University of Minnesota, St. Paul, MN 55108, timgriffis@umn.edu

To be submitted to *Atmospheric Chemistry and Physics*

Abstract:

The atmospheric carbon dioxide (CO_2) mixing ratio and its carbon isotope ($\delta^{13}C$-CO_2) composition contain important CO_2 sink and source information spanning from ecosystem to global scales. The observation and simulation for both CO_2 and $\delta^{13}C$-CO_2 can be used to constrain regional emissions and better understand the anthropogenic and natural mechanisms that control $\delta^{13}C$-CO_2 variations. Such work remains rare for urban environments, especially megacities. Here, we used near-continuous CO_2 and $\delta^{13}C$-CO_2 measurements, from September 2013 to August 2015, and inverse modeling to constrain the CO_2 budget and investigate the main factors that dominated $\delta^{13}C$-CO_2 variations for the Yangtze River Delta (YRD) region, one of the largest anthropogenic CO_2 hotspots and densely populated regions in China. We used the WRF-STILT model framework with category-specified EDGAR v4.3.2 CO_2 inventories to simulate hourly CO_2 mixing ratios and $\delta^{13}C$-CO_2, evaluated these simulations with observations, and constrained the total anthropogenic CO_2 emission. We show that: (1) Top-down and bottom-up estimates of anthropogenic CO_2 emissions agreed well (bias < 6%) on an annual basis; (2) The WRF-STILT model can generally reproduce the observed diel and seasonal atmospheric $\delta^{13}C$-CO_2 variations; (3) Anthropogenic CO_2 emissions played a much larger role than ecosystems in controlling the $\delta^{13}C$-CO_2 seasonality. When excluding ecosystem respiration and photosynthetic discrimination in the YRD area, $\delta^{13}C$-CO_2 seasonality increased from 1.53‰ to 1.66‰; (4) Atmospheric transport processes in summer amplified the cement CO_2 enhancement proportions in the YRD area, which dominated monthly δs (the mixture of $\delta^{13}C$-CO_2 from all regional end-members) variations. These findings support that the combination of long-term atmospheric carbon isotope observations and inverse modeling can provide a powerful constraint on the carbon cycle of these complex megacities.

Keywords: cements production, $^{13}C/^{12}C$ ratio, WRF-STILT model, plant photosynthetic discrimination

1. Introduction

Urban landscapes account for 70% of global CO_2 emissions and represent less than 3% of Earth's land area (Seto et al., 2014). Such CO_2 hotspots play a dominant role in controlling the rise in atmospheric CO_2 concentrations, which exceeded 412 ppm in December 2019 for global monthly average observations (https://www.esrl.noaa.gov/gmd/ccgg/trends/). Furthermore, the carbon isotope ratio of CO_2 (i.e. $\boldsymbol{\delta}^{13}C$ = $^{13}C/^{12}C$ ratio in delta notation) at the representative Mauna Loa site, USA, has steadily decreased to around -8.5‰, in December 2019 (https://www.esrl.noaa.gov/). Anthropogenic CO_2 emission is produced from fossil fuel burning and cement production. As the urban population is expected to increase by 2.5 to 6 billion people in 2050, anthropogenic CO_2 emissions are projected to increase dramatically, especially in developing regions and countries (Sargent et al., 2018; Ribeiro et al., 2019). Under such a scenario, the observations of atmospheric CO_2 and $\boldsymbol{\delta}^{13}C$-$CO_2$ in urban landscapes are of great importance to monitoring these potential CO_2 emissions hotspots (Lauvaux et al., 2016; Nathan et al., 2018; Graven et al., 2018; Pillai et al., 2016; Staufer et al., 2016).

Countries are required to report their CO_2 emissions according to the Intergovernmental Panel on Climate Change guidelines (IPCC, 2019), and many "bottom-up" methods have long been used to estimate CO_2 emissions worldwide, but such methods have high uncertainties for CO_2 emissions at regional (20%) to city (50 to 250%) scales (Gately & Hutyra, 2017; Gately et al., 2015). These large uncertainties are propagated into the estimation of biological fluxes in atmospheric inversions (Zhang et al., 2014; Jiang et al., 2014; Thompson et al., 2016). By using CO_2 observations, the "top-down" atmospheric inversion approach is a useful tool to evaluate "bottom-up" inventories (Graven et al., 2018; L. Hu et al., 2019; Lauvaux et al., 2016; Nathan et al., 2018). Previous research has shown that additional information, such as data on atmospheric $\boldsymbol{\Delta}^{14}CO_2$-$CO_2$, $\boldsymbol{\delta}^{13}C$-$CO_2$, and CO, is needed to better distinguish CO_2 emissions from different sources and to assess their uncertainties (Chen et al., 2017; Graven et al., 2018; Nathan et al., 2018; Cui et al., 2019). The use of hourly $\boldsymbol{\delta}^{13}C$-$CO_2$ observation in urban areas remains rare in inversion studies, yet such observations contain invaluable information of anthropogenic CO_2 from different categories.

Traditional estimates of $\boldsymbol{\delta}^{13}C$-$CO_2$ using isotope ratio mass spectrometry (IRMS) are very limited because flask air sample collection requires long preparation time and is expensive. Consequently, there is a lack of high temporal and long-term observations of $\boldsymbol{\delta}^{13}C$-$CO_2$ (Sturm et al., 2006). Isotope ratio infrared spectroscopy technology (IRIS) has overcome these limitations. As a result, *in situ* air sample analyses using IRIS analyzers are resulting in dense time series of $\boldsymbol{\delta}^{13}C$-$CO_2$. However, most of the established

102   long-term IRMS and IRIS δ^{13}C-CO$_2$ measurement sites are representative of "background", natural, or

103   agricultural ecosystems at locations far away from urban landscapes (Chen et al., 2017; Griffis, 2013).

104   To date, long-term (> 1 year) and continuous observations of both CO$_2$ and δ^{13}C-CO$_2$ have been reported

105   for only five cities, including Bern, Switzerland (Sturm et al., 2006); Boston, USA (McManus et al.,

106   2010); Salt Lake City, USA (Pataki et al., 2006); Beijing, China (Pang et al., 2016); and Nanjing, China

107   (Xu et al., 2017). In these previous investigations, significant diel and seasonal variations of δ^{13}C-CO$_2$

108   have been observed; these patterns were modulated by fossil fuel combustion, plant respiration and

109   photosynthesis, and changes in the height of the atmospheric boundary layer (Sturm et al., 2006; Guha

110   and Ghosh, 2010). No study has quantified the impact of each factor on the seasonal variation of δ^{13}C-

111   CO$_2$. This represents an important knowledge gap in understanding the underlying mechanisms of carbon

112   cycling in complex urban ecosystems.

113   The traditional δ^{13}C-CO$_2$ isotope partitioning methods (including Miller-Tans and the Keeling plot

114   approaches) have been used to constrain different CO$_2$ sources worldwide (Keeling, 1960; Vardag et al.,

115   2015; Newman et al., 2016; Pang et al., 2016; Xu et al., 2017). These methods are based on the

116   assumption that partitioned atmospheric CO$_2$ enhancement components from different sources can

117   represent CO$_2$ emissions at the "target area" (Miller and Tans, 2003; Ballantyne et al., 2011). Carbon

118   dioxide emissions are highly inhomogeneous at the urban scale, with extremely strong point/line sources,

119   and the final partitioning results are highly uncertain without considerations of source footprint

120   characteristics (Gately & Hutyra, 2017; Cui et al., 2019; Martin et al., 2019). Atmospheric transport

121   models can help to resolve such problems, and the coupling of atmospheric transport models with isotope

122   observations have recently been applied in global and regional CO$_2$ partitioning studies (Chen et al., 2017;

123   Cui et al., 2019; Graven et al., 2018; C. Hu et al., 2018b). Although urban CO$_2$ inversions have been

124   applied successfully in several studies in Europe and the United States (Bréon et al., 2015; Turnbull et al.,

125   2015; Pillai et al., 2016; Brioude et al., 2013; Turner et al., 2016), urban CO$_2$ inversions in China are

126   rare (Berezin et al., 2013; C. Hu, 2018a; Worden et al., 2012), presumably because of the scarcity of high

127   quality δ^{13}C-CO$_2$ and CO$_2$ observations.

128   The Yangtze River Delta (YRD) ranks as one of the most densely populated regions in the world and is

129   an important anthropogenic CO$_2$ hotspot. Major anthropogenic sources include the power industry, oil

130   refineries/transformation and cement production. Having the largest source of cement-derived CO$_2$

131   production across China and the world (Cai et al., 2015), the YRD contributed 20% of national cement

132   production, nearly 12% of world's total cement output in 2014 (USGS, 2014; Xu et al., 2017; Yang et al.,

133   2017). In addition to anthropogenic factors, natural ecosystems and croplands act as significant CO$_2$ sinks

134   and sources within the YRD. Independent quantification of the fossil and cement CO$_2$ emission and

135   assessment of their impact on atmospheric δ^{13}C-CO_2 have potential to improve our understanding of

136   urban CO_2 cycling. Further, the observations and simulations of both atmospheric CO_2 and δ^{13}C-CO_2 can

137   help us relate atmospheric CO_2 dynamics with future emission control strategies.

138   Here, we combine long-term (>2 years) CO_2 and δ^{13}C-CO_2 observations with atmospheric transport

139   model simulations to study urban atmospheric CO_2 and δ^{13}C-CO_2 variations. The objectives were to: (1)

140   Constrain anthropogenic CO_2 emissions and determine the main sources of uncertainty for δ^{13}C-CO_2

141   simulations, and (2) Quantify the relative contributions of each factor (i.e. background, anthropogenic

142   CO_2 emissions especially for cement production, ecosystem photosynthesis and respiration) to seasonal

143   variations of atmospheric δ^{13}C-CO_2.

144   2. Materials and methods

145   2.1 Observations of atmospheric CO_2 mixing ratio, δ^{13}C-CO_2 and supporting variables

146   The observation site is located on the Nanjing University of Information Science and Technology campus

147   (hereafter NUIST, $32^{o}12$'N, $118^{o}43$'E, green dot in Figure 1a). Continuous atmospheric CO_2 mixing

148   ratios and δ^{13}C-CO_2 were measured at a height of 34 m above ground with an IRIS analyzer (model

149   G1101-i, Picarro Inc., Sunnyvale, CA). The observation period extended from September 2013 to August

150   2015. Calibrations for CO_2 mixing ratio and δ^{13}C-CO_2 were conducted with standard gases traceable to

151   NOAA/GML (NOAA Global Monitoring Laboratory) standards. Calibration details are provided by Xu et

152   al. (2017). Based on Allan variance analyses, the hourly precisions of CO_2 and δ^{13}C-CO_2 were 0.07 ppm

153   and 0.05‰, respectively. We note that the δ^{13}C-CO_2 IRIS (model G1101-i) measurements are sensitive to

154   water vapor concentration. Sensitivity tests reveal that the δ^{13}C-CO_2 IRIS measurements are biased high

155   (less than 0.74‰) when water vapor mole fraction exceeds 2%. The data presented here have been

156   corrected following the procedures outlined in Xu et al. (2017).

157   We separated the two-year study period into seasons (autumn: September, October, November; winter:

158   December, January, February; spring: March, April, May; summer: June, July, August). Further, for an

159   annual comparison, we examined the period from September 2013 to August 2014 (Year 2014) versus

160   September 2014 to August 2015 (Year 2015).

161   The YRD is a cement production hotspot in China (Figure 1b). It had a total population of 190 million in

162   2018 (Figure 2a) with 24.2 million in the city of Shanghai, 9.8 million in Hangzhou city (provincial

163   capital of Zhejiang), 8.4 million in Nanjing city (provincial capital of Jiangsu), and 8.1 million in Hefei

164   city (provincial capital of Anhui). The CO_2 related production data (i.e. cement) and energy consumption

165   data (i.e. coal and natural gas) were obtained from local official sources using the same method described

166   in Shen et al. (2014).

167 To examine the effects of plant photosynthesis on atmospheric CO_2 variations, we used NDVI

168 (Normalized Difference Vegetation Index), SIF (solar-induced chlorophyll fluorescence) and GPP (gross

169 primary productivity) information. These three products have a global distribution with spatial resolution

170 of 0.05^o by 0.05^o. The NDVI has a temporal resolution of 16 days and SIF and GPP products have a

171 temporal resolution of 8 days (Li & Xiao, 2019; http://globalecology.unh.edu/data/). Land-use and land-

172 cover classification in Yangtze River Delta for 2014 was applied by using NDVI data from MOD13A2.

173 2.2 Simulation of atmospheric $\boldsymbol{\delta}^{13}C$-$CO_2$

174 2.2.1 General equations

175 The simulation of atmospheric $\boldsymbol{\delta}^{13}C$-$CO_2$ is based on mass conservation. First, we briefly describe the

176 simulation of atmospheric CO_2 mixing ratios (more details are provided in Section 2.2.2), following the

177 previous work of Hu et al., (2018b), where atmospheric CO_2 was simulated (CO_{2_sim}) as the sum of

178 background (CO_{2_bg}) and the contribution from all regional sources/sinks ($[\boldsymbol{\Delta}CO_{2\_sim}]_i$), as

179
$$CO_{2\_sim} = CO_{2\_bg} + \sum_{i=1}^{n}[\Delta CO_{2\_sim}]_i \tag{1}$$

180 Note that $\boldsymbol{\Delta}CO_2$ is the sum of all simulated sources/sinks $[\boldsymbol{\Delta}CO_{2\_sim}]_i$ and represents the total simulated

181 CO_2 enhancement. We use $\boldsymbol{\Delta}CO_{2\_obs}$ as the observed CO_2 total enhancement, which can be calculated by

182 using the CO_2 observation minus the CO_2 background values. Based on mass conservation, we estimated

183 the $^{13}CO_2$ composition by multiplying the left- and right-hand sides of equation (1) by $\boldsymbol{\delta}^{13}C$,

184
$$\delta^{13}C_{a\_sim} = \frac{\delta^{13}C_{bg} \times CO_{2\_bg} + \sum_{i=1}^{n}\delta_i^{13} \times [\Delta CO_{2\_sim}]_i}{CO_{2\_sim}} \tag{2}$$

185 where $\boldsymbol{\delta}^{13}C_{a\_sim}$ and $\boldsymbol{\delta}^{13}C_{bg}$ represent the simulated atmospheric $\boldsymbol{\delta}^{13}C$-$CO_2$ and background $\boldsymbol{\delta}^{13}CO_2$, $\boldsymbol{\delta}_i^{13}$ is

186 the $\boldsymbol{\delta}^{13}C$-$CO_2$ for end-member i (including anthropogenic and biological source categories). The $\boldsymbol{\delta}^{13}C$-

187 CO_2 contributions from all regional sources/sinks can be further reformatted as equation 3,

188
$$\sum_{i=1}^{n}\delta_i^{13} \times [\Delta CO_{2\_sim}]_i = \delta_{s\_sim} \times \sum_{i=1}^{n}[\Delta CO_{2\_sim}]_i \tag{3}$$

189 where $\boldsymbol{\delta}_{s\_sim}$ is the simulated enhancement-weighted mean of all regional end-members. We use $\boldsymbol{\delta}_s$ as the

190 observed term to distinguish it from $\boldsymbol{\delta}_{s\_sim}$ (Newman et al., 2008), which will be described in detail in

191 section 2.2.5. The product on the right-hand side of equation 3 is the simulated regional source term that

is added to the background value and contains both enhancement and δ^{13}C-CO$_2$ signals contributed by different CO$_2$ sources/sinks. This product can also be treated as an observed term when using the derived δ_{s_obs} and observed ΔCO$_{2\_obs}$ values.

To date, there are no available global δ^{13}C-CO$_2$ background products and the choice of δ^{13}C$_{bg}$ is essential to simulating δ^{13}C$_a$. Here, we apply three strategies. First, we used discrete δ^{13}C-CO$_2$ flask observations at Mount Waliguan (hereafter WLG, 36°17'N, 100°54'E; https://www.esrl.noaa.gov/gmd/dv/data/) to represent the δ^{13}C-CO$_2$ background signal at our site. These observations were measured at weekly intervals to the end of 2015. A digital filtering curve fitting (CCGCRV) regression method was applied to derive hourly background values following Thoning et al. (1989). There are, however, reasons why WLG may not be an ideal background site for our study domain. For example, based on the previous simulation results for the CO$_2$ background sources, most of the back trajectories originate from the free atmosphere or 1000 m higher above the ground (Hu et al., 2019). Further, the footprint at the north/west edge of Domain 1 is relatively small, indicating that most back trajectories were observed above the planetary boundary layer height (hereafter PBLH). Here, the WLG observations were made near the surface. Further, WLG is not located at the border of our simulation domain 1. Therefore, the strong vertical δ^{13}C-CO$_2$ gradients between the boundary layer and the free tropospheric atmosphere (Chen et al., 2006; Guha et al., 2010; Sturm et al., 2013) can cause a low bias in the δ^{13}C-CO$_2$ background when using this approach.

In the second approach, the δ^{13}C-CO$_2$ background signal was estimated with wintertime "clean" air CO$_2$ and δ^{13}C-CO$_2$ observations at the NUIST site, using the following equation

$$\delta^{13}C_{bg} = \frac{\delta^{13}C_a \times CO_2 - \sum_{i=1}^{n} \delta_i^{13} \times [\Delta CO_{2\_sim}]_i}{CO_{2\_bg}}$$

(4)

where δ^{13}C$_a$ and CO$_2$ represent atmospheric δ^{13}C-CO$_2$ and CO$_2$ observations at the NUIST site under clean conditions. Note that δ^{13}C$_a$ represents the observed δ^{13}C-CO$_2$ not the simulated δ^{13}C-CO$_2$ (δ^{13}C$_{a\_sim}$) as shown in equation 2. [ΔCO$_{2\_sim}$]$_i$ is the simulated category-specified CO$_2$ enhancements. We defined clean conditions as the bottom 5% wintertime CO$_2$ observations to minimize simulated CO$_2$ enhancement errors from both biological and anthropogenic CO$_2$ simulations on δ^{13}C-CO$_2$ background calculation. The CO$_{2\_bg}$ is obtained from heights 1000 m above ground level (see Section 2.2.3).

In the third approach, we avoid the use of modeled [ΔCO$_{2\_sim}$]$_i$ results and replaced the simulated regional source term in equation 4 with observed $\delta_{s\_obs} \times \Delta$CO$_{2\_obs}$, as described in equation 3, and used the Miller-

Tans regression method to calculate monthly δ_{s_obs}. This approach does not require simulation of $[\Delta CO_2]_i$ or the corresponding $\delta^{13}C$-CO_2 signals. The hourly $\delta^{13}C$-CO_2 background value can be derived by using δ_{s_obs}, CO_2 background, observed atmospheric $\delta^{13}C_a$ and CO_2 (see details in Section 2.3 and supplement materials). Comparison of these three strategies will be evaluated and discussed in Section 3.2.1. Similar methods used to derive other background tracers have included CO_2 (Alden et al., 2016; Verhulst et al., 2017), CO (Wang et al., 2010; Ruckstuhl et al., 2012) and CH_4 (Zhao et al., 2009; Verhulst et al., 2017; Hu et al., 2019). To analyze the controlling factors for the $\delta^{13}C$-CO_2 seasonality, the CCGCRV (a digital filtering curve fitting program developed by the Carbon Cycle Group, NOAA, USA) regression was applied to the background, observations, and simulations. Finally, we derived CCGCRV curve fitting lines by using 11 regressed parameters, which were based on the hourly time series of observations/simulations, and defined the difference between peak and trough in one year as the seasonality of $\delta^{13}C$-CO_2.

2.2.2 Simulation of atmospheric CO_2 mixing ratios

In equation 1, the CO_{2_bg} is obtained from the Carbon Tracker 2016 product, which provides global CO_2 distributions from the ground level up to a height of 50 km. We used the averaged concentration above the latitude and longitude where the released particles entered the study domain 1 (Figure 1a). The variable ΔCO_{2_sim} was derived by multiplying the simulated hourly footprint function with the hourly CO_2 fluxes (Hu et al., 2018a; b). Considering the diurnal variations of both anthropogenic and biological CO_2 fluxes, 168 footprints were obtained representing each simulated hour. This accounted for the back trajectory of particle movement for 168 hours (i.e. 24 hours per day for 7 days) of transport. The 168 footprints are multiplied by the corresponding hourly CO_2 flux. The CO_2 fluxes contain anthropogenic CO_2 emissions, biological CO_2 flux and biomass burning. Here the anthropogenic CO_2 emission sources include power industry, combustion for manufacturing, non-metallic minerals production (cement), oil refineries/transformation industry, energy for building and road transportation. Theoretically, ΔCO_{2_sim} represents the CO_2 changes contributed by every pixel within the simulated domain. As shown by Hu et al. (2018a), most of the ΔCO_{2_sim} is contributed by sink/source activity within the YRD area. In order to quantify the relative contributions within the YRD area, we separated the study domain into 5 zones based on provincial administrative boundaries including Jiangsu, Anhui, Zhejiang, Shanghai, and the remaining area outside the YRD (Figure 2). The modeled CO_2 was calculated as follows:

$$\Delta CO_{2\_sim} = \sum_{i=1}^{168} flux_i \times footprint_i \tag{5}$$

251 where $flux_i$ (units: mol m^{-2} s^{-1}) corresponds to each CO_2 flux category simulated for each domain for a

252 specific hour i, and footprint (units: ppm m^2 s/µmol) is the model simulated sensitivity of observed CO_2

253 enhancement to flux changes in each pixel. The i contains the hourly footprint during trajectory of particle

254 movement for 168 hours as described above. The CO_2 enhancement from each of the 5 zones were

255 simulated by multiplying CO_2 emissions in each province with the corresponding footprint.

256 2.2.3 WRF-STILT model configuration

257 The Stochastic Time-Inverted Lagrangian Transport (hereafter STILT) model was used to generate the

258 above footprint, which is defined as the sensitivity of atmospheric CO_2 enhancement to the upwind flux at

259 the receptor site (observation site). The meteorological fields used to drive the STILT model were

260 simulated with the Weather Research and Forecasting Model (WRF3.5) at high spatial and temporal

261 resolutions. The innermost nested domain (D3, 3 km × 3 km, Figure 1) contains the YRD area, where the

262 most sensitive footprint is located, and the intermediate domain (D2, 9 km × 9 km) and outermost (D1, 27

263 km × 27 km) represent Eastern China and Central and Eastern China, respectively. The same physical

264 schemes and parameter setup for the WRF meteorological fields simulation and the Domain in the STILT

265 model have been used previously for inverse analyses (Hu et al., 2019). These previous studies at the

266 NUIST observation site have shown very good performance in simulating the meteorological fields,

267 which is essential for reliable STILT simulations. The hourly footprint was simulated by releasing 500

268 particles from the NUIST measurement site and tracking their backward locations every 5 minutes for a

269 period of 7 days. Particle numbers and their residence time within half of the PBLH were used to

270 calculate the footprint over the 7 day period. For the CO_2 background of each hour, we tracked the

271 sources of air particles back trajectory for 7 days, and defined these CO_2 mixing ratios in Carbon Tracker

272 as the hourly CO_2 background values (Peters et al., 2007).

273 2.2.4 A priori anthropogenic CO_2 emissions and net ecosystem exchange

274 The Emission Database for Global Atmospheric Research (EDGAR v4.3.2) inventory was selected as the

275 *a priori* anthropogenic CO_2 emissions (Figure 2a), which is based on the International Energy Agency's

276 (IEA) energy budget statistics and provides detailed CO_2 source maps (29 categories, including both

277 organic and fossil emissions, IEA, 2012) with global coverage at high spatial resolution (0.1^o × 0.1^o). The

278 EDGAR CO_2 emissions are the most up-to-date global inventory with sectoral detail (Janssens-Maenhout

279 et al., 2017; Schneising et al., 2013). Other inventories, including the Fossil Fuel Data Assimilation

280 System (FFDAS, Rayner et al., 2010) and the Open-source Data Inventory for Anthropogenic CO_2

281 (ODIAC, Oda et al., 2018) also provide global CO_2 emissions. However, these inventories only provide

282 total CO_2 emissions or have very limited emission categories, which limit our ability to provide isotope

283   end-member information. EDGAR v4.3.2 provides emission estimates at a monthly time scale. Here, we

284   applied hourly scaling factors for different categories following Hu et al., (2018a). EDGAR v4.3.2 with

285   monthly resolution is available only for 2010. We assume that each CO_2 category changes linearly from

286   its 2010 value (Peters et al., 2007) and apply an annual scaling factor of 1.145 to derive CO_2 emissions for

287   2014 and 2015. This scaling factor is based on Carbon Tracker, dividing the same anthropogenic CO_2

288   emissions for YRD in years 2014-2015 by that in 2010.

289   The biological flux or net ecosystem CO_2 exchange (NEE) and biomass burning CO_2 emissions come

290   from Carbon Tracker *a posteriori* flux at 3-hour intervals and at a spatial resolution of $1^o \times 1^o$. Because

291   NEE is much smaller than the anthropogenic CO_2 emissions in such densely developed urban landscapes,

292   we homogeneously distributed this flux at a spatial resolution of 0.1^o within each grid to match the

293   footprint.

294   2.2.5 Simulation of the carbon isotope ratio of all sources ($\boldsymbol{\delta}_{s\_sim}$)

295   The carbon isotope ratio of all the surface sources was calculated as (Newman et al., 2008):

296

$$\sum_{i=1}^{n} \delta_i \times p_i = \delta_{s\_sim} \tag{6}$$

297   where δ_i is the $\boldsymbol{\delta}^{13}$C-CO_2 value from source category i, and p_i is the corresponding enhancement

298   proportion (i.e. proportions of a specific enhancement i to total CO_2 enhancement). We define $\boldsymbol{\delta}_{s\_sim}$ as the

299   simulated carbon isotope ratio of all sources to differentiate it from the observed $\boldsymbol{\delta}_{s\_obs}$. Based on fossil

300   fuel usage characteristics in YRD, we reassigned the EDGAR v4.3.2 categories according to fuel types.

301   Coal was the fuel type for manufacturing, oil for oil refinery, natural gas for buildings, and diesel and

302   gasoline for transportation. The power industry consumed 5% natural gas and 95% coal based on local

303   activity data in YRD (China statistical Yearbook, 2015). The non-metallic mineral production was mainly

304   for cement. Since there is a lack of detailed information for non-metallic mineral production, we

305   simply attributed 100% of it to cement production. Chemical processes were mainly ammonia

306   synthesis. Based on a literature review and our previous work (Xu et al., 2017), typical $\boldsymbol{\delta}^{13}$C-CO_2 values

307   for natural gas (−39.06‰ ± 1.07‰), coal (−25.46‰ ± 0.39‰), fuel oil (−29.32‰ ± 0.15‰), gasoline

308   (−28.69‰ ± 0.50‰), ammonia synthesis (−28.18‰ ± 0.55‰), and diesel (−28.93‰ ± 0.26‰), pig iron

309   (−24.90‰ ± 0.40‰), crude steel (−25.28‰ ± 0.40‰), cement (0‰ ± 0.30‰), biofuel combustion and

310   biological emissions (−28.20‰ ± 1.00‰) were used in this study. We also applied a value of −28.20‰

311   for photosynthesis (Griffis et al., 2008; Lai et al., 2014) because YRD is a region dominated by C_3 plants.

312   Since CO_2 emissions associated with human respiration (Prairie and Duarte, 2017; Turnbull et al., 2015;

313   Miller et al., 2020) are relatively small (3.7% of anthropogenic emissions in the YRD area, Xu et al.,

314   2017), and given that the local food diet is dominated by C_3 grains that have a similar $\delta^{13}C$-CO_2 value as

315   the biological CO_2 flux of −28.20‰, we assume it has the same isotope signals as local C_3 plants and

316   ecosystem respiration. Further, the biological CO_2 flux from the Carbon Tracker assimilation system

317   considered anthropogenic as fixed and attributed the remainder to the biological CO_2 flux (Peters et al.,

318   2007). Consequently, we believe the uncertainty in the biological CO_2 flux will include the small

319   proportion of human respiration.

320   To evaluate the simulated δ_{s_sim}, we applied the Miller-Tans and Keeling plot approaches to derive δ_{s_obs}

321   from the observed concentration and atmospheric $^{13}CO_2$-CO_2 (Xu et al. 2017). We then used the results to

322   evaluate the calculations made with Equation (6).

323   2.3 Independent IPCC method for anthropogenic CO_2 emissions

324   Large differences among inventories have been previously found even for the same region (Berezin et al.,

325   2013; Andrew, 2019). For comparison with the EDGAR v4.3.2 inventory results, we derived the

326   anthropogenic CO_2 emissions by using an independent IPCC method. Here, we illustrate the calculation

327   for cement CO_2 emissions. Note that the IPCC only recommended an EF for clinker, which is an

328   intermediate product of cement. To calculate cement CO_2 emissions, we need to calculate it based on

329   clinker production, as shown in Equation (7),

$$CO_2[cement] = M_{cement} \times C_{clinker} \times EF_{clinker} \qquad (7)$$

331   where $CO_2[cement]$ is the chemical process CO_2 emissions for cement production, M_{cement} is the

332   production of cement, $C_{clinker}$ represents the clinker to cement ratio (%), and $EF_{clinker}$ is the CO_2 emission

333   factor for clinker production. The IPCC recommended an $EF_{clinker}$ value of 0.52 ± 0.01 tonne CO_2 per

334   tonne clinker produced, where CaO content for clinker is assumed to be 65% with 100% CaO from

335   calcium carbonate material (IPCC 2013). The EF appears to be well constrained, showing little variation

336   among provinces with mean values ranging from 0.512 to 0.525 (Yang et al., 2017). For the $C_{clinker}$ values,

337   it generally showed a decreasing trend from 64.5% in 2004 to 56.9% in 2015 for all of China (Figure S1),

338   with an average value of 57.0% during 2014 and 2015.

339   2.4 Multiplicative scaling factor method

340   To quantify anthropogenic CO_2 emissions and to compare them with EDGAR products, we first derived

341   the monthly scaling factors for anthropogenic CO_2 emissions using a multiplicative scaling factor

342   (hereafter MSF) method (Sargent et al., 2018; He et al., 2020), and then obtained annual averages. The

343   monthly scaling factors (SFs) were calculated as:

344
$$MSF = \frac{CO_{2\_obs} - CO_{2\_bg} - \Delta CO_{2\_bio} - \Delta CO_{2\_fire}}{\Delta CO_{2\_anthro}}$$ (8)

345 where CO_{2_obs}, ΔCO_{2_bio}, ΔCO_{2_fire} and ΔCO_{2_anthro} represent observed CO_2 mixing ratios, simulated CO_2

346 enhancements contributed by biological flux, biomass burning, and anthropogenic emissions, respectively.

347 Uncertainties of all factors on the final MSFs were calculated based on Monte Carlo methods, where the

348 normal sample probability distribution was applied and the upper 97.5% and lower 2.5% of the values

349 was considered as the uncertainty for MSF (Cao et al., 2016).

350 3. Results and Discussion

351 3.1 Evaluation of hourly CO_2 mixing ratios

352 3.1.1 Hourly and monthly CO_2 mixing ratio comparisons

353 This section examines the general performance of simulating hourly CO_2 mixing ratios. The two-year

354 average hourly footprint is shown in Figure 2b where the source area (blue-red) indicates strong

355 sensitivity of the CO_2 observations to regional sources. This footprint shape is representative of the YRD

356 area. To quantify the relative contributions from each province, we calculated CO_2 enhancements

357 contributed by Anhui, Jiangsu, Zhejiang, Shanghai, and the remaining area outside of the YRD,

358 respectively. The results indicate that Jiangsu contributed approximately 80% of the total enhancement

359 (discussed further in Section 3.1.2). Comparisons between simulated and observed hourly CO_2 mixing

360 ratios are displayed in Figure 3a for both years. For all hourly data in each year, the model versus

361 observation correlation coefficient (R) was $R = 0.38$ (n = 8204, P < 0.001) and RMSE = 29.44 ppm for

362 2014, and $R = 0.35$ (n = 7262, P < 0.001) and RMSE = 30.22 ppm for 2015. These results indicate that the

363 model can simulate the synoptic and diel CO_2 variations over the two-year period. The model also

364 captured the monthly and seasonal variations of CO_2 mixing ratios (daily averages are shown in Figure

365 S2). The simulations captured the trend of rising CO_2 mixing ratios after October and the drawdown of

366 CO_2 to the background value during the summer.

367 Figures 3b-d illustrate the average monthly daily, nighttime (22:00-06:00, local time), and daytime

368 (10:00-16:00) CO_2 mixing ratios. These monthly values contain the effects of atmospheric transport,

369 background and variations in CO_2 emissions. The observed and simulated CO_2 mixing ratios showed a

370 significant increase from September 2013 to January 2014. Here, the CO_2 mixing ratios increased by 16.0

371 ppm according to the model results and 17.2 ppm according to the observations. The background values

372 increased by 8.1 ppm and accounted for 47% of the total CO_2 increase, and the net CO_2 flux (*a priori*) for

373 YRD increased by 15%. We attributed the remaining 38% increase to changes in atmospheric transport

374 processes including lower PBLH in January 2014 than in September 2013. To quantify how variations in

PBLH affected CO_2 mixing ratios, we compared the simulated monthly anthropogenic CO_2 enhancement differences in the same months of different years, to eliminate the influence of monthly emission variations on CO_2 enhancements. Twelve monthly paired values were used and are shown in Figure 4. This analysis indicates that atmospheric CO_2 mixing ratios decreased by about 3.7 ppm for an increase of PBLH by 100 m. We also note that there were two months (March and August) that fall far below this trend, implying that changes in the monthly footprints (source area) can also play an important role.

On an annual timescale, the simulated average CO_2 mixing ratios were 436.63 ppm and 437.11 ppm for 2014 and 2015, respectively. Since the anthropogenic CO_2 emissions used in the model are the same for both years, the simulated annual average CO_2 difference can be used to quantify the influence associated with meteorological factors and ecosystem carbon cycling. Between these two years, the CO_2 background increased by 1.78 ppm, the biological enhancement decreased by 1.04 ppm from 2014 to 2015. The remaining 0.26 ppm change between 2014 and 2015 indicates a relatively small meteorological effect for the annual averages, such as a slight change in dominant wind direction or a PBLH difference.

The simulated annual average NEE CO_2 enhancements were 2.64 ppm and 1.60 ppm for the respective years. For comparison, the annual average anthropogenic enhancements were 36.20 ppm and 34.90 ppm for 2014 and 2015, respectively. The monthly NEE enhancement varied from -0.1 ppm in May 2015 to +6.0 ppm July 2014, indicating NEE contributes positively for enhancement in most months (Figure 5a), even though the sign of monthly averaged NEE flux in summer was negative (sinks). This positive contribution was mainly caused by diel PBLH variations between daytime (smaller negative enhancement) and nighttime (larger positive enhancement). To further evaluate the impact of plant photosynthetic activity on the regional CO_2 cycle, we examined the NDVI, SIF and GPP seasonal patterns (Figures 5d-f). These three datasets revealed two peaks during each year, which is related to increased photosynthetic activity. The first peak occurred in May and the second in August-September, corresponding to the growing season of wheat and corn/rice, respectively (Deng et al., 2015). We note that GPP was derived from SIF, and as a result, they share a similar seasonal cycle. The land-use classification in YRD for 2014 (Figure S3) shows that north YRD is dominated by agricultural land and south dominated by forest land, and our observation site was more surrounded by agricultural land which corresponded well with observed NDVI, SIF and GPP seasonal patterns. The peak SIF and GPP signals during the summer were about 20 times greater than during the winter. Consequently, we can ignore the potential influence of photosynthetic activity on the regional CO_2 enhancements during the non-growing seasons.

3.1.2 Components of urban CO_2 enhancement

406   Here, we diagnose the source contributions to the urban CO_2 enhancement. The observed anthropogenic
407   CO_2 enhancements, which were derived by subtracting CO_2 background and simulated biological
408   enhancement from CO_2 concentration observations, were 38.36±3.32 ppm and 37.89±2.80 ppm for 2014
409   and 2015, respectively. Here, the uncertainty of the observed anthropogenic CO_2 enhancements was
410   calculated by prescribing a 2 ppm potential bias for the Carbon Tracker CO_2 fields and 50% to the
411   simulated biological CO_2 enhancement (Hu et al., 2018b). The corresponding simulated anthropogenic
412   CO_2 enhancements were 36.20 ppm and 34.90 ppm. In comparison with the simulated biological CO_2
413   enhancements displayed in Figure 5a, both the observed and simulated CO_2 enhancements are indicative
414   of a large anthropogenic (fossil fuel and cement production) CO_2 emission from the YRD.

415   Previous studies have also investigated urban CO_2 enhancements from a relatively broad range of
416   developed environments worldwide. Verhulst et al. (2017) measured CO_2 mixing ratios at seven sites in
417   Los Angeles, USA and concluded that the mean annual enhancement varied between 2.0 ppm and 30.8
418   ppm, which is considerably lower than our findings. Another study in Washington D.C., USA in February
419   and July 2013 showed that the CO_2 enhancement was less than 20 ppm (Mueller et al., 2018). The urban
420   CO_2 observations and modeling study by Martin et al. (2019) at three urban sites in eastern USA showed
421   an enhancement of ~21 ppm in February 2013, substantially lower (by ~20 ppm) than our observations.
422   The measurements at an urban-industrial complex site in Rotterdam, Netherlands, indicated a CO_2
423   enhancement of only 11 ppm for October to December 2014 (Super et al., 2017). Our enhancements were
424   significantly higher than all of these previous reports of other urban areas.

425   The anthropogenic components and source area contributions are displayed in Figure 5b-c. During the
426   study period the average anthropogenic enhancements were 5.1%, 80.2%, 1.9%, 4.4%, and 8.5% for
427   Anhui, Jiangsu, Zhejiang, Shanghai, and the remaining area outside the YRD, respectively. Although
428   Shanghai's area is the smallest within the YRD region and relatively distant (~300 km) from our
429   observation site, its maximum source contribution at times exceeded 50% (i.e. on 19th September 2013,
430   not shown) *via* long-distance transport. In general, power industry, manufacturing, non-metallic mineral
431   production, oil refinery, and other source categories contributed 41.0%, 21.9%, 9.3%, 11.5%, and 16.3%
432   to the total anthropogenic CO_2 enhancement, respectively. The proportions of corresponding CO_2
433   emission categories to the total anthropogenic emissions of the YRD were 39.8%, 28.4%, 7.4%, 4.1%,
434   and 24.4%, respectively. The comparisons between the proportions of simulated enhancement and
435   proportions of corresponding CO_2 emissions can illustrate whether CO_2 enhancement partitions is a good
436   tracer for emissions in complex urban area. We found a relatively large difference between the
437   enhancement proportion and the emission proportion for oil refineries (from 11.5% to 4.1%) as compared
438   to other categories. This may be because power industry, manufacturing and non-metallic mineral

439 production were more homogeneously distributed compared to oil refineries, which were closer to our

440 CO_2 observation site. Further, changes in source footprint caused by wind direction variations likely

441 played an important role.

442 3.1.3 Constraints on monthly anthropogenic CO_2 emissions

443 To provide a robust comparison of bottom-up CO_2 emissions for YRD, we calculated anthropogenic CO_2

444 emissions from both EDGAR v4.3.2 and with activity data provided by local governments (Table 1) and

445 the default IPCC emission factors (https://www.ipcc-nggip.iges.or.jp/EFDB/). The total anthropogenic

446 CO_2 emissions in 2014-2015 were 24.4×10^{11} kg and 23.5×10^{11} kg according to our own inventory and

447 EDGAR v4.3.2 CO_2, respectively, indicating excellent agreement (within 4%) between these approaches.

448 We constrained the monthly anthropogenic CO_2 emissions by using the MSF method (equation 8) and

449 computed the 12-month average to represent the years of 2014 and 2015. The *a posteriori* results indicate

450 that the annual scaling factors were 1.03 ± 0.10 for 2014 and 1.06 ± 0.09 for 2015. The monthly scaling

451 factors derived from using daytime and all-day observations are also shown in Figure S4. These factors

452 vary seasonally with higher values observed in summer. When using daytime values only, the scaling

453 factors were much larger than the all-day values. This can be seen in Figure 3 by comparing the simulated

454 and observed CO_2 mixing ratios. We should note here that the larger scaling factors based on the daytime

455 data could be caused by bias in the *a priori* daily scaling factors used to generate the hourly CO_2

456 emissions (Hu et al., 2018b); the monthly anthropogenic averages; and bias in negative biological CO_2

457 enhancement. Since our study is mainly focused on the seasonality of all-day observations, the monthly

458 scaling factors derived from the all-day approach will be used for the following analyses. The

459 anthropogenic CO_2 emissions in year 2015 did not show a significant change compared to 2014, and the

460 overall estimates were within the uncertainty of the estimates. After applying the average scaling factors

461 for 2014 and 2015, the *a posteriori* anthropogenic CO_2 emissions were $24.6 (\pm 2.4) \times 10^{11}$ kg for the YRD

462 area. The application of the MSF method provides an overall constraint on the anthropogenic CO_2

463 emissions (also displayed in Table 1).

464 The main uncertainties associated with the simulation of hourly CO_2 and $\boldsymbol{\delta}^{13}$C-CO_2 are uncertainty in

465 meteorological fields, transport model (i.e. number of released particles), and *a priori* CO_2 fluxes. At the

466 annual scale the main uncertainty is attributed to the PBLH simulations and *a priori* anthropogenic CO_2

467 emissions. The anthropogenic CO_2 emissions biases were $< 6\%$ as described above, and the bias

468 associated with PBLH uncertainty was typically $<13\%$ (Hu et al., 2018a; 2018b). There, we attribute a 20%

469 uncertainty to the simulated CO_2 and $\boldsymbol{\delta}^{13}$C-CO_2 signals on an annual time scale.

470 3.2 Simulation of atmospheric $\boldsymbol{\delta}^{13}$C-CO_2

471   3.2.1 Background atmospheric δ^{13}C-CO$_2$

472   To obtain the best representative δ^{13}C-CO$_2$ background value for the study domain we examined the

473   values from the three strategies described above (Figure 6). We also compared the δ^{13}C-CO$_2$ at the WLG

474   background site with observations at NUIST during winters (Figure S5). This was performed to help

475   simplify the comparison by removing the effects of plant photosynthetic discrimination. The δ^{13}C-CO$_2$ at

476   the WLG site was relatively more depleted in the heavy carbon isotope (or negative, by up to 0.5‰) than

477   that observed at NUIST for many periods. Theoretically, there are two key factors that can cause the

478   urban atmospheric δ^{13}C-CO$_2$ to be relatively more enriched in the heavy carbon isotope (or positive)

479   compared to the background values including: 1) Discrimination associated with ecosystem

480   photosynthesis; and 2) Enrichment of isotopic signature associated with the CO$_2$ derived from cement

481   production. As shown earlier, the biological CO$_2$ enhancement was positive in winter, which implies a

482   positive biological CO$_2$ signal where ecosystem respiration is more important than photosynthesis.

483   Further, sensitivity tests for cement CO$_2$ sources showed its influence is much smaller than the observed

484   difference in Figure S5 (discussed in section 3.3.3). Based on the above analyses and methods introduced

485   in Section 2.3, we concluded that the WLG δ^{13}C-CO$_2$ signal is not an ideal choice for representing the

486   background value. The wintertime δ^{13}C-CO$_2$ background values, based on strategy 2, were -7.78‰ and -

487   7.61‰ for 2013-2014 and 2014-2015, respectively (Figure 6). The corresponding values, based on

488   strategy 3, were -7.70‰ and -7.53‰. These background values are more enriched compared to the WLG

489   observations by 0.80‰ to 1.01‰. These derived values agree well with the monthly δ^{13}C-CO$_2$ simulation

490   results of Chen et al. (2006) who showed that δ^{13}C-CO$_2$ is 0.6‰ higher above the PBL than in the surface

491   layer near the ground. Recently, Ghasemifard et al. (2019) showed that hourly δ^{13}C-CO$_2$ values at Mount

492   Zugspitze, the highest (2650 m) mountain in Germany, varied between -7‰ and -12‰ in the winter for

493   2013. During two especially clean air events (in October and February) at Mount Zugspitze, the δ^{13}C-CO$_2$

494   was approximately -7‰, during which the CO$_2$ mixing ratios varied between 390 and 395 ppm. This is

495   consistent with our estimates using strategies 2 and 3. Based on the evidence presented above, we believe

496   that strategy 3 is the most robust way to derive a background δ^{13}C-CO$_2$ for the study domain.

497   3.2.2 Evaluation of δ^{13}C-CO$_2$ simulations

498   Figure 7a shows the hourly δ^{13}C-CO$_2$ simulations over a two-year period. To the best of our knowledge,

499   this is the first time that δ^{13}C-CO$_2$ has been simulated at an hourly time scale for an urban region. The

500   simulations are consistent with the observations at daily, monthly and annual time scales, where the

501   average value of observations (simulations) were -8.69‰ (-8.68‰) and -8.52‰ (-8.45‰) for 2014 and

502   2015, respectively. The corresponding correlation was R = 0.54 ($P < 0.001$) and R = 0.52 ($P < 0.001$).

503   The root mean square error between observations and simulations was 1.07‰ for 2014 and 1.10‰ for

504   2015 (Table 2). Further, the observed and simulated δ^{13}C-CO_2 values showed seasonal variations that

505   increased in summer and decreased in winter. This pattern mirrored the CO_2 mixing ratios for both

506   observations and simulations (Figures 3a and 8). Similar relations and seasonal variations of δ^{13}C-CO_2

507   have been reported in other urban areas (Sturm et al., 2006; Guha & Ghosh, 2010; Moore & Jacobson,

508   2015; Pang et al., 2016). The simulated hourly NEE CO_2 enhancement is also shown in Figure 7b. Note

509   that negative values indicate net CO_2 sinks and positive values indicate net CO_2 sources. We can see large

510   hourly variations in the growing seasons and positive enhancements during nighttime that are generally

511   larger than negative enhancements during daytime. This shows the potential influence of NEE on δ^{13}C-

512   CO_2 seasonality. To date, no study has quantified the relative contributions to the δ^{13}C-CO_2 seasonality.

513   Here, we re-evaluate and quantify the main factors contributing to its seasonality based on the

514   combination of δ^{13}C-CO_2 observations and simulations in the following section.

515   Here, we examine the comparisons for winter and summer in greater detail. The simulations showed that

516   the model can generally capture the diel variations of observed hourly δ^{13}C-CO_2 variations (Figure 8).

517   Statistics between observations and simulations for two seasons are shown in Table 2. The observed

518   seasonal average increased substantially, by 1.18‰, from winter 2013-2014 (-9.27‰) to summer 2014 (-

519   8.09‰). The simulations showed a similar seasonal increase of 1.35‰. Some large discrepancies are

520   evident and generally caused by the simulated total CO_2 enhancement biases (potentially caused by

521   poorly simulated PBLH during these periods) and the negative relationship between δ^{13}C-CO_2 and the

522   CO_2 enhancement as shown in Figure S6.

523   Comparisons between observations and simulations for daily average CO_2 mixing ratio and δ^{13}C-CO_2 are

524   also shown in Figure 9. Although the data are distributed around the 1:1 line for both seasons, there is less

525   scatter and higher correlation in the winter than in the summer. We attributed this to the more complex

526   biological CO_2 sinks in the summer, which are not adequately resolved by the relatively coarse model

527   grid (1° by 1°). We also performed comparisons by only choosing the daytime observations. The results

528   indicated that daytime CO_2 mixing ratio simulations in the summer were slightly underestimated. This

529   caused δ^{13}C-CO_2 to be overestimated (Figure S7). The simulations for winter generally captured the

530   trends for both CO_2 and δ^{13}C-CO_2 when the biological CO_2 enhancement played a relatively small role

531   compared to anthropogenic emissions. The larger bias in the summer could result from the relatively

532   coarse spatial-temporal resolution (aggregation error) of the Carbon Tracker biological CO_2 flux, which

533   was 1×1 degree with three-hour average. As shown in Figure S3, the spatial distribution of land use is far

534   more heterogeneous. This will smooth the stronger biological CO_2 signals by averaging it over the large

535   1×1 degree grid, while the urban biological CO_2 flux occurs at much finer spatial scales and likely varies

536   at shorter time intervals.

537   3.2.3 Mechanisms controlling the $\delta^{13}C$-CO_2 seasonality

538   The mechanisms driving these seasonal variations are examined below. The peak and trough in the

539   observed $\delta^{13}C$-CO_2 signal was observed in December and July (Figure 10a), respectively, yielding an

540   amplitude of 1.51‰. This was consistent with the simulated amplitude of 1.53‰. These results support

541   that the simulated $\delta^{13}C$-CO_2 seasonality agreed well with the observations (Figure 10), and can be used to

542   further diagnose the mechanisms contributing to the $\delta^{13}C$-CO_2 seasonality. According to equation 2, the

543    $\delta^{13}C$-CO_2 seasonality can be attributed to four factors including: (1) A change in the background $\delta^{13}C$-

544   CO_2 value from -7.64‰ in December to -6.66‰ in July; (2) A change in CO_2 background from 399 ppm

545   to 398 ppm; (3) The total CO_2 enhancement change from 45.7 ppm to 37.3 ppm; and (4) The change in

546   the isotope composition of the CO_2 enhancements causing δs to vary from -26.1‰ to -22.8‰.

547   To quantify each mechanism's contribution to the seasonality of atmospheric $\delta^{13}C$-CO_2, we recalculated

548    $\delta^{13}C$-CO_2 by using the monthly averages as described above. First, we calculated $\delta^{13}C$-CO_2 in December

549   and July, which were -9.54‰ and -8.04‰, respectively, with amplitude of 1.50‰. Next, we replaced the

550    $\delta^{13}C$-CO_2 background value in December (-7.64‰) with July (-6.67‰). The recalculated $\delta^{13}C$-CO_2 was -

551   8.66‰ in December, indicating that the change in $\delta^{13}C$-CO_2 background value caused a change of 0.88‰

552   (9.54‰ minus -8.66‰) to the seasonality. By changing both the total CO_2 enhancement and background

553   values, the recalculated $\delta^{13}C$-CO_2 was -8.32‰, contributing a 0.34‰ change in the seasonality (-8.66‰

554   minus -8.32‰). Finally, by changing δs from -26.1‰ to -22.8‰, together with the change in background

555   value, the recalculated $\delta^{13}C$-CO_2 was -8.32‰ a change of 0.34‰ (i.e. -8.66‰ minus -8.32‰). This

556   indicates that both the total CO_2 enhancement and change in δs contributed equally to the regional source

557   term, causing a variation of 0.62‰ (i.e. 1.50‰ minus 0.88‰). Based on the above analyses, we attributed

558   59% and 41% of the $\delta^{13}C$-CO_2 seasonality to the changing $\delta^{13}C$ background term and regional source

559   terms, respectively. Further, the total CO_2 enhancement and change in δs, sum of both can be treated as

560   regional source term, contributed equally (about 20%) to the $\delta^{13}C$-CO_2 seasonality.

561   To investigate how ecosystem photosynthetic discrimination and respiration affected atmospheric $\delta^{13}C$-

562   CO_2 seasonality, we simulated the $\delta^{13}C$-CO_2 again for two cases: (1) excluding negative NEE when

563   photosynthesis is stronger than respiration, and (2) excluding both photosynthetic discrimination and

564   respiration. Note that only NEE was used in our study with no partitioning between photosynthesis and

565   respiration in the daytime. The only role of photosynthetic discrimination should be stronger than in case

566   1 when only negative NEE is used. The results are shown in Figure 10 b-c. Overall, the negative CO_2

567   enhancement caused atmospheric δ^{13}C-CO$_2$ to become more enriched in the baseline simulations with

568   maximum values around 1‰ between April and October (Figure 10b), and positive CO$_2$ enhancement (i.e.

569   via net respiration) caused atmospheric δ^{13}C-CO$_2$ to become more depleted compared to the baseline

570   simulations through the whole year (Figure 10c). By applying the CCGRCV fitting technique to the δ^{13}C-

571   CO$_2$ for the above two cases, we found that the δ^{13}C-CO$_2$ seasonality decreased to 1.45‰ in case 1,

572   indicating ecosystem photosynthetic discrimination explained > 0.08‰ of the seasonality (1.53‰ minus

573   1.45‰). For case 2, the δ^{13}C-CO$_2$ trough in winter slightly increased by 0.08‰ and peak in summer

574   increased by 0.20‰, these two factors finally lead the seasonality increase to 1.66‰, which were caused

575   by much larger respiration CO$_2$ enhancement in summer than in winter (Figure 7b). These results indicate

576   that biological respiration reduced the δ^{13}C-CO$_2$ seasonality by 0.20‰, and that negative NEE

577   (photosynthetic discrimination) acted to increase the δ^{13}C-CO$_2$ seasonality by 0.08‰. Generally, both

578   ecosystem photosynthesis and respiration played minor roles in controlling the atmospheric δ^{13}C-CO$_2$

579   seasonality within this urban area. In other words, the anthropogenic CO$_2$ emissions played a much larger

580   role than the plants.

581   As shown in Figure 5, CO$_2$ sources from power industry, combustion for manufacturing, non-metallic

582   mineral production and oil refineries and transformation industry were the top 4 contributors to the CO$_2$

583   enhancements. We simulated atmospheric δ^{13}C-CO$_2$ by assuming that no CO$_2$ was emitted from each of

584   these 4 categories. The simulations were performed by excluding one category at a time. The results

585   indicated that atmospheric δ^{13}C-CO$_2$ seasonality was 1.30‰, 1.57‰, 1.30‰, and 1.47‰, if excluding

586   power industry, combustion for manufacturing source, oil refineries/transformation industry, and non-

587   metallic mineral production sources, respectively. In other words, power industry and oil refineries/

588   transformation industry together contributed 0.40‰ to the total regional source term of 0.62‰. The

589   cement sources played a role in enriching 0.07‰ the atmospheric δ^{13}C-CO$_2$ in the heavy isotope, contrary

590   to all other anthropogenic CO$_2$ sources.

591   3.3 Sensitivity analysis

592   3.3.1 Comparison of δs·ΔCO$_2$

593   Based on equation 2, the regional source term determines the hourly/daily variations of δ^{13}C-CO$_2$, which

594   is treated as a signal added to the background signal. To evaluate the model simulated regional source

595   term with respect to the observations we examined daily averages for winter to minimize the influence of

596   photosynthesis. In Figure 11a, the observed daily δs·ΔCO$_2$ values are compared with the simulated values

597   using the *a priori* anthropogenic CO$_2$ emissions. Here ΔCO$_2$ represents the total CO$_2$ enhancement for

598   both observations and simulations. The product δs·ΔCO$_2$ can be interpreted as the regional source term.

599   The average values were -1009.0 (and -841.9) ppm·‰ for observations and -1096.7 (and 1000.5) ppm·‰

600   for model results in 2014 (and 2015). The slope of the regression fit was 0.99 (±0.12) and the intercept

601   was -151.7 (±130.1) for all data during the two winters. After applying the monthly scaling factors to

602   constrain the anthropogenic CO_2 emissions, the re-calculated results were closer to the 1:1 line with a

603   slightly improved correlation (R increased from 0.47 to 0.50; Figure 11b). Note that the application of the

604   monthly scaling factors only impacts the $\boldsymbol{\Delta}CO_2$ but not $\boldsymbol{\delta}$s. The uncertainty in $\boldsymbol{\delta}$s will be discussed next.

605   3.3.2 Comparison between δ_{s_sim} and δ_s

606   To evaluate the $\boldsymbol{\delta}_s$ simulations, we compared observed and simulated $\boldsymbol{\delta}_s$ as displayed in Figure 12a for all-

607   day and nighttime conditions. Here, nighttime simulations were selected to minimize the effects of

608   ecosystem photosynthesis and to mainly focus on the anthropogenic CO_2 sources. Two methods were

609   used to calculate $\boldsymbol{\delta}_s$ from the observations including the Miller-Tans and Keeling plot methods. Although

610    $\boldsymbol{\delta}_s$ differed between these two methods, both displayed similar seasonal variations with higher values

611   ($\boldsymbol{\delta}^{13}C$ enrichment) in summer and lower values in winter. Such seasonal variations were also observed at

612   other urban sites including Beijing, China (Pang et al., 2016), Bern, Switzerland (Sturm et al., 2006),

613   Bangalore city, India (Guha and Ghosh, 2010),Wroclaw, Poland (Górka and Lewicka-szczebak, 2013).

614   If the CO_2 sources/sinks are homogeneously distributed and without monthly variations, the atmospheric

615   CO_2 enhancement components would remain unchanged, and there would be no seasonal changes in $\boldsymbol{\delta}_s$.

616   In reality, variations in atmospheric transport processes interact with regional CO_2 sink/source changes

617   that cause monthly variations in $\boldsymbol{\delta}_s$. The comparison of $\boldsymbol{\delta}_s$ between simulations and observations indicated

618   that the model performed well in capturing the mixing and transport of CO_2 from different sources. We

619   can also infer from their difference that the proportions of some CO_2 categories were biased in the *a*

620   *priori* emission map. This can be caused by both the downscaling of EDGAR inventory distribution to

621    $0.1°$ and the magnitude of some emissions categories. Among all anthropogenic sources, the most

622   significant linear relations were found between the simulated anthropogenic $\boldsymbol{\delta}_s$ and cement CO_2

623   proportions for these 24 months, with slopes of 0.33‰ for nighttime and 0.35‰ for all-day conditions (R^2

624   = 0.97, p < 0.001; Figure 12 b & c). These results also indicated that cement CO_2 emissions dominated

625   monthly $\boldsymbol{\delta}$s variations in the YRD region.

626   3.3.3 Sensitivity of atmospheric $\boldsymbol{\delta}^{13}C$-$CO_2$ and $\boldsymbol{\delta}_s$ to cement CO_2 emissions

627   The discrepancy between simulated and observed $\boldsymbol{\delta}_s$ highlights that some CO_2 sources were biased in the

628   *a priori* inventories. As discussed above, cement CO_2 emissions had the most distinct $\boldsymbol{\delta}^{13}C$-$CO_2$ end-

629   member value of 0‰ ± 0.30‰ when compared with the averages of other anthropogenic sources.

630   Combined with its large emission compared to other regions of the world, it had a strong potential to

631   influence δ_s and $\delta^{13}C$-CO_2. YRD represents the largest cement producing region in the world (USGS,

632   2014; Cai et al., 2015; Yang et al., 2017). Its relative proportion to total national anthropogenic CO_2

633   emissions is about 5.5% to 6.5% based on IPCC method and 7.3% for EDGAR. These proportions are 50%

634   greater than the global average of 4% (Boden et al., 2016) and much larger than most countries (Andrew,

635   2018) and other large urbanized areas such as California (2%; Cui et al., 2019).

636   The local activity data reveals that the cement production increased from 3.55×10^8 tons in 2010 to $4.56 \times$

637   10^8 tons in 2014 in the YRD area. Our own calculation of the national clinker-to-cement indicated a

638   decreasing trend from 64% in 2004 to around 56% in 2015. Here, we applied the value of 61.7% for 2010

639   and the average value of 57.0% for 2014 to 2015. We then used the EF for clinker (0.52 ± 0.01 tonne CO_2

640   per tonne clinker; IPCC 2013). Finally, the calculated cement CO_2 emissions were 1.14 ($\pm$ 0.02) $\times 10^8$

641   tonne for 2010 and 1.35 ($\pm$0.03) $\times 10^8$ tonne for 2014, indicating an 18.4% increase over this time period.

642   This result is close to the scaling factor 1.145 for the total anthropogenic CO_2 emissions for the same

643   period.

644   The cement CO_2 emission was 1.45×10^8 tonne for the EDGAR products in 2010. Applying the scaling

645   factor of 1.184, based on our independent method, the EDGAR cement CO_2 emissions was 1.72×10^8

646   tonne for the year of 2014. The 27% difference between the EDGAR inventory and our independent

647   calculations probably resulted from large errors in the clinker-to-cement ratio and regional activity data.

648   Ke et al. (2013) reported a much higher clinker-to-cement ratio of 73% to 70% for China during 2005 and

649   2007 than the ratio of 57% in 2014 to 2015. If we applied a 70% ratio, the EDGAR cement CO_2 emission

650   would change to 1.28×10^8 tonne for 2010.

651   The monthly cement emission proportions varied from 6.21% to 8.98%, while its enhancement proportion

652   was much larger and could reach 16.85%. In other words, favorable atmospheric transport processes

653   amplified the cement CO_2 enhancement proportion at our observational site (Table S2). To quantify the

654   extent to which the cement CO_2 enhancement components can affect δs and atmospheric $\delta^{13}C$-CO_2 we

655   conducted sensitivity tests by changing the cement enhancement proportions to 0.8, 1.2, 1.4, 1.6, 1.8, and

656   2 times its original value. These sensitivity tests are based on two different assumptions for cement CO_2

657   enhancement changes: (1) There is no bias in the total anthropogenic CO_2 enhancement such that a

658   proportional increase/decrease in the cement component does not change the relative anthropogenic

659   contributions; (2) Only the cement enhancement changes. From equation 2, these two assumptions will

660   change both δs and $\delta^{13}C$-CO_2 but with different amplitude.

Results for the first assumption are shown in Figure 13a-b for both nighttime and all-day δ_s simulations. The simulated δ_s increased linearly with the increase of cement proportions, at a rate of 2.73‰ increase per 10% increase of cement proportions in the nighttime and 2.72‰ for all-day. The result for the second assumption is similar to the first one, yielding a 2.32‰ increase for a 10% increase in the cement proportion. As shown in Table S2, the cement CO_2 enhancement proportions increased from 5.60% - 6.77% (December) to 13.16% - 16.85% (June), which is the primary cause for the observed monthly δ_s variations. The high sensitivity of δ_s to cement CO_2 proportions can partly explain the relative difference of modeled δ_s and indicates a potential advantage to constrain cement CO_2 emissions by using atmospheric $\delta^{13}C$-CO_2 observations. Finally we calculated how cement CO_2 can change atmospheric $\delta^{13}C$-CO_2 (Figure 13c). These results show that atmospheric $\delta^{13}C$-CO_2 is more sensitive to the first assumption than the second assumption. These sensitivity analyses indicate that a cement CO_2 enhancement relative change of 20% (or absolute 1.57% increase) can cause a 0.013‰ - 0.038‰ change in the atmospheric $\delta^{13}C$-CO_2. These results indicate that δ_s is sensitive to cement CO_2 emissions.

4 Conclusions

(1) Total annual anthropogenic CO_2 emissions for the YRD showed high consistency between the top-down and bottom-up approaches with a bias less than 6%.

(2) Approximately 59% and 41% of the $\delta^{13}C$-CO_2 seasonality was attributed to the change in $\delta^{13}C$ background value and the regional CO_2 source term, respectively.

(3) Power industry and oil refineries/ transformation industry together contributed 0.40‰ to the seasonal cycle, accounting for 64.5% in all regional source terms (0.62‰).

(4) If excluding all ecosystem respiration and photosynthetic discrimination in YRD area, $\delta^{13}C$-CO_2 seasonality will increase from 1.53‰ to 1.66‰.

(5) Atmospheric transport processes in summer amplified the cement CO_2 enhancement proportions in the YRD area, which dominated monthly δ_s variations. δ_s calculated from simulations was shown to be a strong linear relation with cement CO_2 EDGAR v4.3.2 inventory proportion in the YRD area.

Acknowledgements

This work is supported by the National Key R&D Program of China (grants 2020YFA0607501 & 2019YFA0607202), Cheng Hu acknowledges support from the Natural Science Foundation of Jiangsu Province (BK20200802), this work is also supported by National Natural Science Foundation of China (grant no.42021004), Natural Science Foundation of Jiangsu Province (BK20181100), and Key Research Foundation of Jiangsu Meteorological Society (KZ201803).

Code/Data availability

693 The data presented in this manuscript has been uploaded on our group website:

694 https://yncenter.sites.yale.edu/data-access.

695 Author contribution: Cheng Hu, Timothy J. Griffis and Xuhui Lee designed the study, Cheng Hu

696 performed the model simulation and wrote the original draft, Supervision: Timothy J. Griffis and

697 Xuhui Lee, Data acquisition: Jiaping Xu, Wenjing Huang, Dong Yang, Yan Chen, Cheng Liu,

698 Shoudong Liu, and Lichen Deng, all co-authors contributed to the data analysis.

699 Competing interests: The authors declare that they have no conflict of interest.

700

701 References:

702 Alden, C. B., Miller, J. B., and Gatti, L. V.: Regional atmospheric CO_2 inversion reveals seasonal and geographic
703 differences in Amazon net biome exchange, *Global Change Biology*, 22, 3427–3443,
704 https://doi.org/10.1111/gcb.13305, 2016.

705 Andrew, R. M.: Global CO_2 emissions from cement production, *Earth System Science Data*, 10, 2213–2239.
706 https://doi.org/10.5194/essd-2017-77, 2018.
707 Ballantyne, A. P., Miller, J. B., Baker, I. T., Tans, P. P., and White, J. W. C.: Novel applications of carbon isotopes
708 in atmospheric CO_2: what can atmospheric measurements teach us about processes in the biosphere? *Biogeosciences*,
709 8, 3093– 3106, https://doi.org/10.5194/bg-8-3093-2011, 2011.

710 Boden, T., Andres, R., and Marland, G.: Global, Regional, and National Fossil-Fuel CO_2 Emissions (1751 - 2013)
711 (V. 2016) [Data set]. Environmental System Science Data Infrastructure for a Virtual Ecosystem; Carbon Dioxide
712 Information Analysis Center (CDIAC), Oak Ridge National Laboratory (ORNL), Oak Ridge, TN (United States).

713 Berezin, E. V., Konovalov, I. B., Ciais, P., Richter, A., Tao, S., Janssens-Maenhout, G., Beekmann, M., and Schulze,
714 E.-D.: Multiannual changes of CO_2 emissions in China: indirect estimates derived from satellite measurements of
715 tropospheric NO_2 columns, Atmos. Chem. Phys., 13, 9415–9438, https://doi.org/10.5194/acp-13-9415-2013, 2013.

716 Brioude, J., Angevine, W. M., Ahmadov, R., Kim, S.-W., Evan, S., McKeen, S. A., Hsie, E.-Y., Frost, G. J.,
717 Neuman, J. A., Pollack, I. B., Peischl, J., Ryerson, T. B., Holloway, J., Brown, S. S., Nowak, J. B., Roberts, J. M.,
718 Wofsy, S. C., Santoni, G. W., Oda, T., and Trainer, M.: Top-down estimate of surface flux in the Los Angeles Basin
719 using a mesoscale inverse modeling technique: assessing anthropogenic emissions of CO, NO_x and CO_2 and their
720 impacts, Atmos. Chem. Phys., 13, 3661–3677, https://doi.org/10.5194/acp-13-3661-2013, 2013.

721 Bréon, F. M., Broquet, G., Puygrenier, V., Chevallier, F., Xueref-Remy, I., Ramonet, M., Dieudonné, E., Lopez, M.,
722 Schmidt, M., Perrussel, O., and Ciais, P.: An attempt at estimating Paris area CO_2 emissions from atmospheric
723 concentration measurements, Atmos. Chem. Phys., 15, 1707–1724, https://doi.org/10.5194/acp-15-1707-2015, 2015.

724 Cao, C., Lee, X., Liu, S., Schultz, N., Xiao, W., Zhang, M., and Zhao, L.: Urban heat islands in China enhanced by
725 haze pollution. *Nature Communications*, 7(1), doi: 10.1038/ncomms12509, 2016.

726 Chen, B., Chen J., Tans, P., and Huang L.: Simulating dynamics of $\delta^{13}C$ of CO_2 in the planetary boundary layer over
727 a boreal forest region : covariation between surface fluxes and atmospheric mixing, *Tellus*, 537–549,
728 https://doi.org/10.1111/j.1600-0889.2006.00213.x, 2006.

729 Chen, J. M., Mo, G., and Deng, F.: A joint global carbon inversion system using both CO2 and 13CO2 atmospheric
730 concentration data, Geosci. Model Dev., 10, 1131–1156, https://doi.org/10.5194/gmd-10-1131-2017, 2017.

731   Cai B., Wang J., He J., and Geng Y.: Evaluating CO_2 emission performance in China's cement industry: An
732   enterprise perspective. *Applied Energy*, 2015.11.006, https://doi.org/10.1016/j.apenergy.2015.11.006, 2015.

733   Cui, X., Newman, S., Xu, X., Andrews, A. E., Miller, J., Lehman, S.: Atmospheric observation-based estimation of
734   fossil fuel CO_2 emissions from regions of central and southern California. *Science of the Total Environment*, 664,
735   381–391, https://doi.org/10.1016/j.scitotenv.2019.01.081, 2019.

736   Deng L., Liu S., and Zhao X., Study on the change in land cover of Yangtze River Delta based on MOD13A2 data,
737   *China Science Paper*, 000(015):1822-1827 (in Chinese).

738   Gately, C. K., Hutyra, L. R., and Wing, I. S.: Cities, traffic, and CO_2 : A multidecadal assessment of trends, drivers ,
739   and scaling relationships, *Proceedings of the National Academy of Sciences of the United States of America*, 112(16),
740   4999–5004, https://doi.org/10.1073/pnas.1421723112, 2015.

741   Gately, C. K., and Hutyra, L. R.: Large uncertainties in urban-scale carbon emissions. *Journal of Geophysical
742   Research: Atmospheres*, 122, 11,242–11,260, https://doi.org/10.1002/2017JD027359, 2017.

743   Ghasemifard, H., Vogel, F. R., Vardag, et al. Pollution Events at the High-Altitude Mountain Site Zugspitze-
744   Schneefernerhaus (2670 m a.s.l.), Germany[J]. Atmosphere, 2019, 10(6).

745   Graven, H. D., Fischer, M. L., Lueker, T., Jeong, S., Guilderson, T. P., Keeling, R.: Assessing fossil fuel CO_2
746   emissions in California using atmospheric observations and models. *Environmental Research Letters*, 13(2018)
747   065007, https://doi.org/ 10.1088/1748-9326/aabd43, 2018.

748   Griffis, T. J., Sargent, S., Baker, J., Lee, X., Tanner, B., Greene, J., Swiatek, E., and K. Billmark K.: Direct
749   measurement of biosphere-atmosphere isotopic CO_2 exchange using the eddy covariance technique, *Journal of
750   Geophysical Research: Atmospheres*, 113, D08304, 2008.

751   Griffis, Timothy J.: Tracing the flow of carbon dioxide and water vapor between the biosphere and atmosphere : A
752   review of optical isotope techniques and their application. *Agricultural and Forest Meteorology*, 174–175, 85–109,
753   2013.

754   Górka, M., and Lewicka-Szczebak, D.: One-year spatial and temporal monitoring of concentration and carbon
755   isotopic composition of atmospheric CO_2 in a Wroclaw (SW Poland) city area. *Applied Geochemistry, 35:7-13,*
756   https://doi.org/10.1016/j.apgeochem.2013.05.010, 2013.

757   Guha, T., and Ghosh, P.: Diurnal variation of atmospheric CO_2 concentration and $\delta^{13}C$ in an urban atmosphere
758   during winter-role of the Nocturnal Boundary Layer. *Journal of Atmospheric Chemistry*, 65(1), 1–12, https://doi.org/
759   10.1007/s10874-010-9178-6, 2010.

760   Hu, C., Liu, S., Wang, Y., Zhang, M., Xiao, W., Wang, W., and Xu, J.: Anthropogenic CO_2 emissions from a
761   megacity in the Yangtze River Delta of China. *Environmental Science and Pollution Research*, 25(23), 23157–
762   23169, https://doi.org/10.1007/s11356-018-2325-3, 2018a.

763   Hu, C., Griffis, T. J., Liu, S., Xiao, W., Hu, N., Huang, W., Yang D., and Lee X.: Anthropogenic methane emission
764   and its partitioning for the Yangtze River Delta region of China. *Journal of Geophysical Research: Biogeosciences*,
765   124, https://doi.org/10.1029/2018JG004850, 2019.

766   Hu, C., Griffis, T. J., Lee, X., Millet, D. B., Chen, Z., Baker, J. M., and Xiao, K.: Top-Down constraints on
767   anthropogenic CO_2 emissions within an agricultural-urban landscape. *Journal of Geophysical Research:
768   Atmospheres*, 123(9), 4674–4694, https://doi.org/10.1029/2017JD027881, 2018b.

769   Hu, L., Andrews, A. E., Thoning, K. W., Sweeney, C., Miller, J. B., Michalak, A. M.: Enhanced North American
770   carbon uptake associated with El Niño. *Science Advances*, 5, eaaw0076, https://doi.org/10.1126/sciadv.aaw0076,
771   2019.

He, J., Naik, V., Horowitz, L. W., Dlugokencky, E., and Thoning, K.: Investigation of the global methane budget over 1980–2017 using GFDL-AM4.1, Atmos. Chem. Phys., 20, 805–827, https://doi.org/10.5194/acp-20-805-2020, 2020.

IPCC (Intergovernmental Panel on Climate Change): 2019 Refinement to the 2006 IPCC Guidelines for National Greenhouse Gas Inventories, available at: https://www.ipcc-nggip.iges.or.jp/ public/2019rf/ (last access: 24 April 2021), 2019

IEA, 2012. CO_2 Emissions from Fuel Combustion 1971–2010, 2012 Edition. International Energy Agency (IEA), Paris 2012.

Janssens-Maenhout, G., Crippa, M., Guizzardi, D., Muntean, M., Schaaf, E., Dentener, F.: EDGAR v4.3.2 Global Atlas of the three major Greenhouse Gas Emissions for the period 1970-2012. Earth System Science Data Discussions, (August), 1–55. https://doi.org/10.5194/essd-2017-79, 2017.

Jiang, F., Wang, H. M., Chen, J. M., Machida, T., Zhou, L. X., Ju, W. M., Matsueda, H., and Sawa, Y.: Carbon balance of China constrained by CONTRAIL aircraft CO_2 measurements, Atmos. Chem. Phys., 14, 10133–10144, https://doi.org/10.5194/acp-14-10133-2014, 2014.

Ke J., Mcneil M., Price L., and Zhou N.: Estimation of CO_2 emissions from China's cement production: Methodologies and uncertainties[J]. *Energy Policy*, 57:172-181, https://doi.org/10.1016/j.enpol.2013.01.028, 2013.

Keeling, C. D.: The concentration and isotopic abundances of carbon dioxide in the atmosphere. Tellus, 12(2), 200–203. Keeling, C. D. (1961). The concentration and isotopic abundances of carbon dioxide in rural and marine air. *Geochimica et Cosmochimica Acta*, 24(3-4), 277–298, https://doi.org/10.1111/j.2153-3490.1960.tb01300.x, 1960.

Lai, C., Ehleringer, J. R., Tans, P., and Wofsy, S. C.: Estimating photosynthetic ^{13}C discrimination in terrestrial CO_2 exchange from canopy to regional scales, *Global Biogeochemical Cycles*, 18, GB1041, https://doi.org/1010.1029/2003gb002148, 2014.

Li, X., and Xiao, J.: A global, 0.05-degree product of solar-induced chlorophyll fluorescence derived from OCO-2, MODIS, and reanalysis data. *Remote Sensing*, 11, 517, https://doi.org/10.3390/rs11050517, 2019.

Lauvaux, T., Miles, N. L., Deng, A., Richardson, S. J., Cambaliza, M. O., Davis, K. J., and Wu K.: High-resolution atmospheric inversion of urban CO_2 emissions during the dormant season of the Indianapolis flux experiment (INFLUX). *Journal of Geophysical Research: Atmospheres*, 121(10), 5213–5236, https://doi.org/10.1002/2015JD024473, 2016.

Martin, C. R., Zeng, N., Karion, A., Mueller, K., Ghosh, S., Lopez-coto, I.: Investigating sources of variability and error in simulations of carbon dioxide in an urban region. *Atmospheric Environment*, 199, 55–69, https://doi.org/10.1016/j.atmosenv.2018.11.013, 2019.

Moore, J., & Jacobson, A. D. (2015). Seasonally varying contributions to urban CO_2 in the Chicago , Illinois , USA region : Insights from a high-resolution CO_2 concentration and δ^{13}C record, *Elementa: Science of the Anthropocene*, 3:000052.

Mueller, K., Yadav, V., Lopez-Coto, I., Karion, A., Gourdji, S., Martin, C., and Whetstone, J.: Siting Background Towers to Characterize Incoming Air for Urban Greenhouse Gas Estimation: A Case Study in the Washington, DC/Baltimore Area. *Journal of Geophysical Research: Atmospheres*, 123(5), 2910–2926, https://doi.org/10.1002/2017JD027364, 2018.

McManus, J.B., Nelson, D.D., Zahniser, M.S.: Long-term continuous sampling of $^{12}CO_2$, $^{13}CO_2$ and $^{12}C^{18}O^{16}O$ in ambient air with a quantum cascade laser spectrometer. *Isotopes in Environmental and Health Studies*, 46:1, 49-63, https://doi.org/10.1080/10256011003661326, 2010.

Miller, J. B., Tans, P. P., White, J. W. C., Conway, T. J., and Vaughn, B. W.: The atmospheric signal of terrestrial carbon isotopic discrimination and its implication for partitioning carbon fluxes, *Tellus B*, 55, 197–206, https://doi.org/10.1034/j.1600-0889.2003.00019.x, 2003.

Miller JB, Lehman SJ, Verhulst KR, Miller CE, Duren RM, Yadav V, Newman S, and Sloop CD. Large and seasonally varying biospheric CO2 fluxes in the Los Angeles megacity revealed by atmospheric radiocarbon. Proc Natl Acad Sci U S A, 2020; 117 (43) 26681-26687; doi.org/10.1073/pnas.2005253117.

Nathan, B., Lauvaux, T., Turnbull, J. C., and Richardson, S.: Source Sector Attribution of CO_2 Emissions Using an Urban CO/CO_2 Bayesian Inversion System. *Journal of Geophysical Research: Atmospheres*, 123, 13611-13621, https://doi.org/10.1029/2018JD029231, 2018.

Newman, S., Xu, X., Affek, H. P., Stolper, E., and Epstein S.: Changes in mixing ratio and isotopic composition of CO_2 in urban air from the Los Angeles basin, California, between 1972 and 2003, *Journal of Geophysical Research*, 113, D23304, https://doi.org/10.1029/2008JD009999, 2008.

Newman, S., Xu, X., Gurney, K. R., Hsu, Y. K., Li, K. F., Jiang, X., Keeling, R., Feng, S., O'Keefe, D., Patarasuk, R., Wong, K. W., Rao, P., Fischer, M. L., and Yung, Y. L.: Toward consistency between trends in bottom-up CO_2 emissions and top-down atmospheric measurements in the Los Angeles megacity, Atmos. Chem. Phys., 16, 3843–3863, https://doi.org/10.5194/acp-16-3843-2016, 2016.

Oda, T., Maksyutov, S., and Andres, R. J.: The Open-source Data Inventory for Anthropogenic CO_2, version 2016 (ODIAC2016): a global monthly fossil fuel CO_2 gridded emissions data product for tracer transport simulations and surface flux inversions, Earth Syst. Sci. Data, 10, 87–107, https://doi.org/10.5194/essd-10-87-2018, 2018.

Pang, J., Wen, X., and Sun, X.: Mixing ratio and carbon isotopic composition investigation of atmospheric CO_2 in Beijing, China. *Science of the Total Environment*, 539, 322–330, https://doi.org/10.1016/j.scitotenv.2015.08.130, 2016.

Peters, W., Jacobson, A. R., Sweeney, C., Andrews, A. E., Conway, T. J., Masarie, K., John B. M., Lori M. P. B., Gabrielle P., Adam I. H., Douglas E. J. W., Guido R. v., James T. R., Paul O. W., Maarten C. K., and Pieter P. T.: An atmospheric perspective on North American carbon dioxide exchange: CarbonTracker. *Proceedings of the National Academy of Sciences*, 104(48), 18925–18930, https://doi.org/10.1073/pnas.0708986104, 2007.

Pataki, D. E., Bowling, D. R., Ehleringer, J. R., and Zobitz, J. M.: High resolution atmospheric monitoring of urban carbon dioxide sources, *Geophysical Research Letter*, 33, L03813, https://doi.org/10.1029/2005GL024822, 2006.

Pillai, D., Buchwitz, M., Gerbig, C., Koch, T., Reuter, M., Bovensmann, H., Marshall, J., and Burrows, J. P.: Tracking city CO_2 emissions from space using a high-resolution inverse modelling approach: a case study for Berlin, Germany, Atmos. Chem. Phys., 16, 9591–9610, https://doi.org/10.5194/acp-16-9591-2016, 2016.

Prairie, Y. T. and Duarte, C. M.: Direct and indirect metabolic CO2 release by humanity, Biogeosciences, 4, 215–217, doi:10.5194/bg-4-215-2007, 2007.

Ruckstuhl, A. F., Henne, S., Reimann, S., Steinbacher, M., Vollmer, M. K., O'Doherty, S., Buchmann, B., and Hueglin, C.: Robust extraction of baseline signal of atmospheric trace species using local regression, Atmos. Meas. Tech., 5, 2613–2624, https://doi.org/10.5194/amt-5-2613-2012, 2012.

Rayner, P. J., Raupach, M. R., Paget, M., Peylin, P., and Koffi, E.: A new global gridded data set of CO2 emissions from fossil fuel combustion : Methodology and evaluation, Journal of Geophysical Research: Atmospheres. 115, D19306, https://doi.org/10.1029/2009JD013439, 2010.

Ribeiro, H. V, Rybski, D., and Kropp, J. P.: Effects of changing population or density on urban carbon dioxide emissions. Nature Communications, (2019), 1–9, https://doi.org/10.1038/s41467-019-11184-y, 2019.

854 Sargent, M., Barrera, Y., Nehrkorn, T., Hutyra, L. R., Gately, C. K., Mckain, K., Sweeney, C., Hegarty, J.,
855 Hardiman, B., Steven C. Wofsy, S. C.: Anthropogenic and biogenic CO_2 fluxes in the Boston urban region,
856 Proceedings of the National Academy of Sciences of the United States of America. 115(40),
857 https://doi.org/10.1073/pnas.1803715115, 2018.

858 Schneising, O., Heymann, J., Buchwitz, M., Reuter, M., Bovensmann, H., and Burrows, J. P.: Anthropogenic carbon
859 dioxide source areas observed from space: assessment of regional enhancements and trends, Atmos. Chem. Phys.,
860 13, 2445–2454, https://doi.org/10.5194/acp-13-2445-2013, 2013.

861 Staufer, J., Broquet, G., Bréon, F.-M., Puygrenier, V., Chevallier, F., Xueref-Rémy, I., Dieudonné, E., Lopez, M.,
862 Schmidt, M., Ramonet, M., Perrussel, O., Lac, C., Wu, L., and Ciais, P.: The first 1-year-long estimate of the Paris
863 region fossil fuel CO2 emissions based on atmospheric inversion, Atmos. Chem. Phys., 16, 14703–14726,
864 https://doi.org/10.5194/acp-16-14703-2016, 2016.

865 Sturm, P., Leuenberger, M., Valentino, F. L., Lehmann, B., and Ihly, B.: Measurements of CO2, its stable isotopes,
866 O2/N2, and 222Rn at Bern, Switzerland, Atmos. Chem. Phys., 6, 1991–2004, https://doi.org/10.5194/acp-6-1991-
867 2006, 2006.

868 Sturm, P., Tuzson, B., Henne, S., and Emmenegger, L.: Tracking isotopic signatures of CO2 at the high altitude site
869 Jungfraujoch with laser spectroscopy: analytical improvements and representative results, Atmos. Meas. Tech., 6,
870 1659–1671, https://doi.org/10.5194/amt-6-1659-2013, 2013.

871 Super, I., Denier van der Gon, H. A. C., van der Molen, M. K., Sterk, H. A. M., Hensen, A., and Peters, W.: A
872 multi-model approach to monitor emissions of CO2 and CO from an urban–industrial complex, Atmos. Chem. Phys.,
873 17, 13297–13316, https://doi.org/10.5194/acp-17-13297-2017, 2017.

874 State Statistical Bureau. China Statistical Yearbook 2015; China Statistical Press: Beijing, China, 2016. (In Chinese)

875 Seto, K. C., Dhakal, S., Bigio, A., Blanco, H., Delgado, G. C., and Dewar, D.: Human settlements, infrastructure,
876 and spatial planning. In O. Edenhofer, et al. (Eds.), Climate change 2014: Mitigation ofclimate change. Contribution
877 ofworking group III to the fifth assessment report of the intergovernmental panel on climate change (pp. 923–1000).
878 Cambridge, UK and New York, NY, USA: Cambridge University Press.
879 https://doi.org/10.1017/CBO9781107415416.018, 2014.

880 Thompson, R. L., Patra, P. K., Chevallier, F., Maksyutov, S., Law, R. M., Ziehn, T., and Ciais P.: Top-down
881 assessment of the Asian carbon budget since the mid 1990s. Nature Communications, 7, 1–10,
882 https://doi.org/10.1038/ncomms10724, 2016.

883 Turnbull, J. C., Sweeney, C., Karion, A., Newberger., T., Lehman, S. J., Tans P. P., Davis, K.: Toward
884 quantification and source sector identification of fossil fuel CO2 emissions from an urban area: results from the
885 influx experiment. Journal of Geophysical Research: Atmospheres, 120(1, 292):–312,
886 https://doi.org/10.1002/2014JD022555, 2015.

887 Turner, A. J., Shusterman, A. A., McDonald, B. C., Teige, V., Harley, R. A., and Cohen, R. C.: Network design for
888 quantifying urban CO2 emissions: assessing trade-offs between precision and network density, Atmos. Chem. Phys.,
889 16, 13465–13475, https://doi.org/10.5194/acp-16-13465-2016, 2016.

890 Thoning, K. W., Tans, P. P., and Komhyr, W. D.: Atmospheric carbon dioxide at Mauna Loa observatory 2.
891 Analysis of the NOAA/GMCC data, 1974–1985. *Journal of Geophysical Research: Atmospheres*, 94(D6), 8549–
892 8565, https://doi.org/10.1029/JD094iD06p08549 ,1989.

893 USGS (U. S. Geological Survey), 2014. Mineral Commodity Summaries 2013.http://minerals.usgs.gov/

894 minerals/pubs/commodity/cement/.

895   Wang, Y., Munger, J. W., Xu, S., McElroy, M. B., Hao, J., Nielsen, C. P., and Ma, H.: CO_2 and its correlation with
896   CO at a rural site near Beijing: implications for combustion efficiency in China, Atmos. Chem. Phys., 10, 8881–
897   8897, https://doi.org/10.5194/acp-10-8881-2010, 2010.

898   Zhang, H. F., Chen, B. Z., van der Laan-Luijkx, I. T., Chen, J., Xu, G., Yan, J. W., Zhou, L. X., Fukuyama, Y., Tans,
899   P. P., and Peters W.: Net terrestrial CO_2 exchange over China during 2001–2010 estimated with an ensemble data
900   assimilation system for atmospheric CO_2, *Journal of Geophysical Research: Atmospheres*, 119, 3500–3515,
901   https://doi.org/10.1002/2013JD021297, 2014.

902   Vardag, S. N., Gerbig, C., Janssens-Maenhout, G., and Levin, I.: Estimation of continuous anthropogenic CO_2:
903   model-based evaluation of CO_2, CO, $\delta^{13}C(CO_2)$ and $\Delta^{14}C(CO_2)$ tracer methods, Atmos. Chem. Phys., 15, 12705–
904   12729, https://doi.org/10.5194/acp-15-12705-2015, 2015.

905   Verhulst, K. R., Karion, A., Kim, J., Salameh, P. K., Keeling, R. F., Newman, S., Miller, J., Sloop, C., Pongetti, T.,
906   Rao, P., Wong, C., Hopkins, F. M., Yadav, V., Weiss, R. F., Duren, R. M., and Miller, C. E.: Carbon dioxide and
907   methane measurements from the Los Angeles Megacity Carbon Project – Part 1: calibration, urban enhancements,
908   and uncertainty estimates, Atmos. Chem. Phys., 17, 8313–8341, https://doi.org/10.5194/acp-17-8313-2017, 2017.

909   Worden, H. M., Cheng, Y., Pfister, G., Carmichael, G. R., Zhang, Q., Streets, D. G.: Satellite-based estimates of
910   reduced CO and CO_2 emissions due to traffic restrictions during the 2008 Beijing Olympics, *Geophysical Research*
911   *Letters*, 39, 1–6, https://doi.org/10.1029/2012GL052395, 2012.

912   Xu, J., Lee, X., Xiao, W., Cao, C., Liu, S., Wen, X., Xu, J., Zhang, Z., and Zhao, J.: Interpreting the $^{13}C/^{12}C$ ratio of
913   carbon dioxide in an urban airshed in the Yangtze River Delta, China, Atmos. Chem. Phys., 17, 3385–3399,
914   https://doi.org/10.5194/acp-17-3385-2017, 2017.

915   Yang, Y., Wang, L., Cao, Z. Mou C., Shen, L.,Zhao, J.,and Fang, Y.: CO_2 emissions from cement industry in China:
916   A bottom-up estimation from factory to regional and national levels. *Journal of Geographical Science,* 27, 711–730.

917   Zhao, C., Andrews, A. E., Bianco, L., Eluszkiewicz, J. Hirsh, A., Macdonald, C., Nehrkorn, T., and Fischer M. L.,.
918   Atmospheric inverse estimates of methane emissions from Central California. *Journal of Geophysical Research*:
919   *Atmospheres*, 2009, 114(D16): 4723-4734, https://doi.org/10.1029/2008JD011671, 2009.

920

921

922

923

924

925

926

927

928

929 Figure 1. (a) Weather Research and Forecasting Model simulation domains and the location of WLG site , the different region
930 colors represent three domains, (b) cement production distribution in YRD and Eastern China. Both green dot in (a) and red star
931 in (b) are NUIST observation site.

932 Figure 2. (a) Annual anthropogenic CO_2 emissions for study domain (units: mol m^{-2} s^{-1}) and population density in 4 megacities
933 (units: people per hectare) including Nanjing, Hefei, Zhejiang, and Shanghai for the year of 2015, (b) Two-year average
934 concentration footprint (units: ppm m^2 s/μmol).

935 Figure 3. (a) Comparisons of hourly CO_2 mixing ratios between observations and model simulation from September 2013 to
936 August 2015, and monthly averages for (b) whole day, (c) nighttime (22:00-06:00, local time) and (d) daytime (10:00 - 16:00);
937 Model results (red), observations (black), and background (grey).

938 Figure 4. Relation between monthly PBLH and change in CO_2 mixing ratio, here these dots represent difference of monthly
939 averages in two different years for all hours.

940 Figure 5. (a) Comparisons of simulated and observed CO_2 enhancement, note 'model' represents the sum of both anthropogenic
941 and biological CO_2 enhancement simulations, (b) CO_2 enhancement contributions from different provinces, (c) simulated
942 anthropogenic CO_2 enhancement proportion for the main sources; Time series (2013 to 2015) of (d) NDVI, (e) SIF, and (f) GPP.
943 The distance indicates the radius of area centered with NUIST observation site, and the NDVI, SIF, GPP values are averages in
944 these areas.

945 Figure 6. Comparisons among three strategies for calculating the background δ^{13}C-CO_2 . Strategy 1 (WLG discrete: weekly
946 discrete observations at WLG site, WLG CCGCRV: derived hourly data with WLG observations and CCGCRV method);
947 Strategy 2 (Calculated: by choosing clean air in winter); and strategy 3 (M-T method: derived results with observations and M-T
948 approach, M-T CCGCRV: derived hourly results with M-T approach and CCGCRV method, see details in section 2.2.1).

949 Figure 7. (a) Comparisons of observed and modeled hourly δ^{13}C-CO_2 from September 2013 to August 2015, where the grey line
950 represent derived δ^{13}C-CO_2 background, and (b) Simulated hourly biological CO_2 enhancement. The shade and lines in both
951 subfigures represent the periods for winter and summer, respectively.

952 Figure 8. Comparisons of observed and modeled (a) CO_2 mixing ratio and (b) δ^{13}C-CO_2 from December 2013 to February 2014;
953 (c) CO_2 mixing ratio and (b) δ^{13}C-CO_2 from December 2014 to February 2015; (e) CO_2 mixing ratio and (f) δ^{13}C-CO_2 from
954 June 2014 to August 2014; (g) CO_2 mixing ratio and (h) δ^{13}C-CO_2 from June 2015 to August 2015.

955 Figure 9. Scatter plots of observed versus modeled (a) winter time CO_2 mixing ratios, (b) winter time δ^{13}C-CO_2, (c) summer time
956 CO_2, and (d) summer time δ^{13}C-CO_2 for both years, here these dots are daily averages.

957 Figure 10. Digital filtering curve fitting (CCGCRV) for background, observations, normal simulations, case 1 (excluding
958 negative NEE when photosynthesis is stronger than respiration), and case 2 (excluding respiration and photosynthesis) in both
959 years, (b) δ^{13}C-CO_2 comparisons between normal simulations and case 1, and (c) δ^{13}C-CO_2 comparisons between normal
960 simulations and case 2.

961 Figure 11. Comparisons of winter time δs·ΔCO_2 using (a) *a priori* and (b) constrained anthropogenic CO_2 emissions.

962 Figure 12. (a) Comparisons between observed and modeled δ_s, (b) relationship between cement CO_2 enhancement proportion and
963 simulated anthropogenic δs for nighttime and (c) all-day.

964
965
966
967
968
969

Figure 13. Sensitivity tests showing the influence of cement CO_2 emissions on $\boldsymbol{\delta}_s$ for (a) nighttime, (b) all-day, and (c) the relation between cement CO_2 and $\boldsymbol{\delta}^{13}C$ for simulation strategies 1 (There is no bias in the total anthropogenic CO_2 enhancement such that a proportional increase/decrease in the cement component does not change the relative anthropogenic contributions) and 2 (only the cement enhancement changes). Note that the numbers in brackets indicate changes in $\boldsymbol{\delta}^{13}C$ with cement CO_2 enhancement proportion (the fraction of cement CO_2 enhancement to simulated total CO_2 enhancement) increase by 0.2 times. The x-axis values indicate changing cement enhancement proportions to 0.8 1.2, 1.4, 1.6, 1.8, and 2 times the original values.

970

971

972

973

974

975

976

977

978

979

980

981

982

983

984
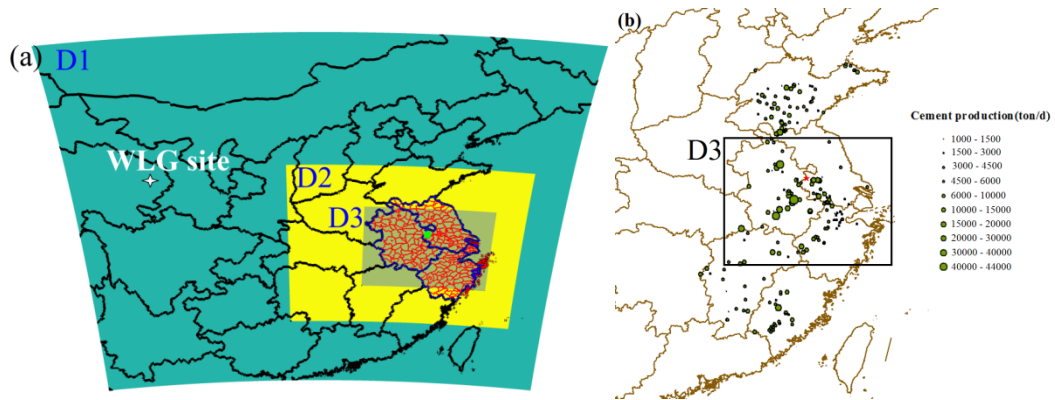
985

986

987 Figure 1. (a) Weather Research and Forecasting Model simulation domains and the location of WLG site , the different region

988 colors represent three domains, (b) cement production distribution in YRD and Eastern China. Both green dot in (a) and red star

989 in (b) are NUIST observation site.

990

991

992

993

994

995

996

997

998

999

1000

1001

1002

1003

1004

1005

1006

1007

1008

1009

1010

Figure 2. (a) Annual anthropogenic CO_2 emissions for study domain (units: mol m^{-2} s^{-1}) and population density in 4 megacities

(units: people per hectare) including Nanjing, Hefei, Zhejiang, and Shanghai for the year of 2015, (b) Two-year average

concentration footprint (units: ppm m^2 s/µmol).

1024
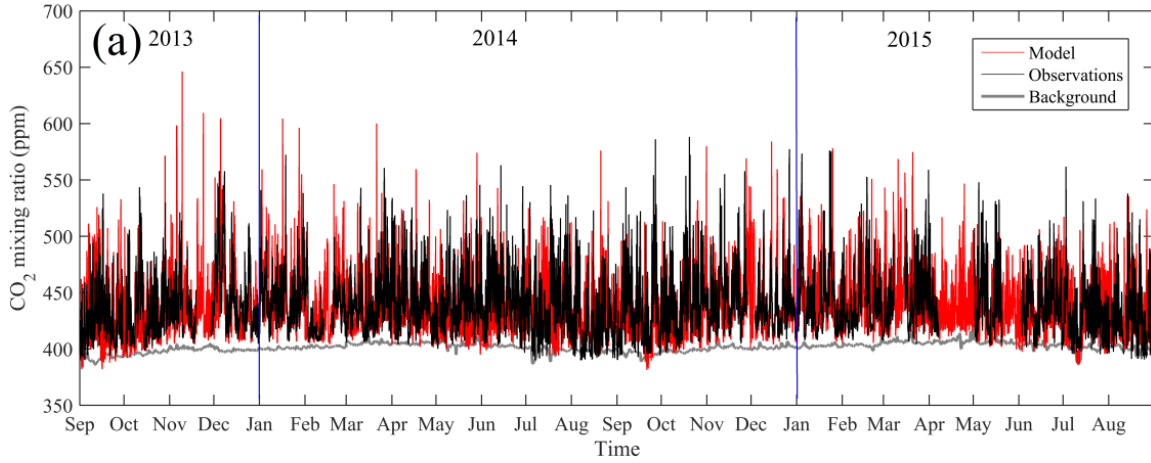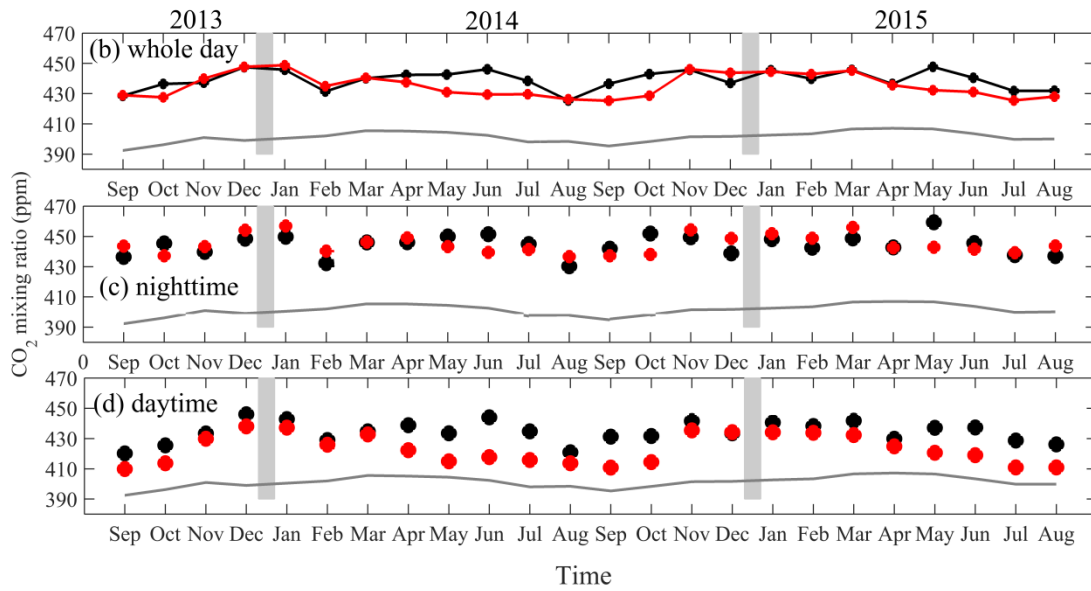
1025

Figure 3. (a) Comparisons of hourly CO_2 mixing ratios between observations and model simulation from September 2013 to
August 2015, and monthly averages for (b) whole day, (c) nighttime (22:00-06:00, local time) and (d) daytime (10:00 - 16:00);
Model results (red), observations (black), and background (grey).

1029

1030
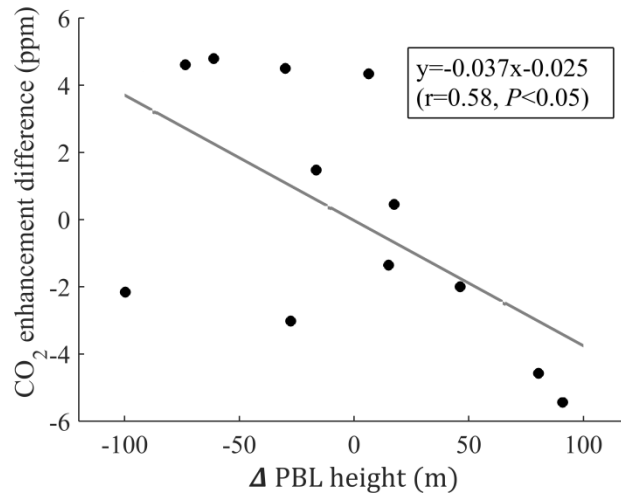
1031

1032 Figure 4. Relation between monthly PBL height and change in CO_2 mixing ratio, here these dots represent difference of monthly

1033 averages in two different years for all hours.

1034

1035

1036

1037

1038

1039

1040

1041

1042
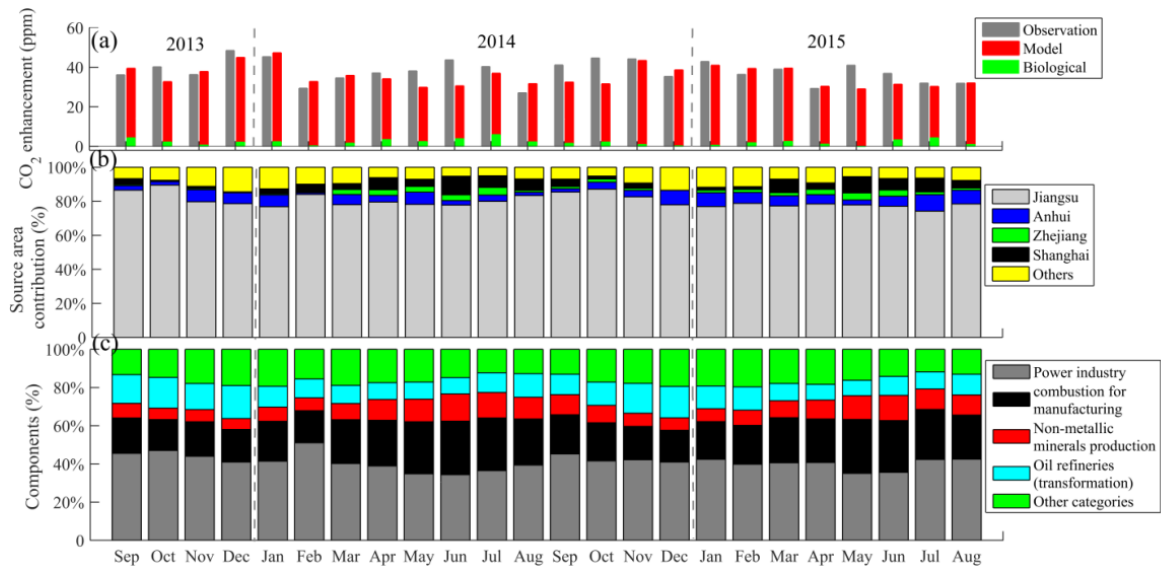
1043
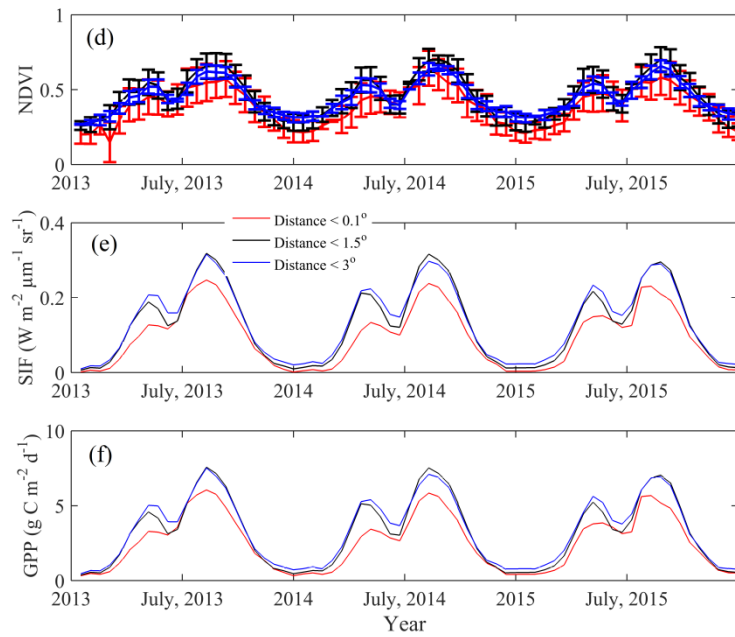
1044

Figure 5. (a) Comparisons of simulated and observed CO_2 enhancement, note 'model' represents the sum of both anthropogenic

and biological CO_2 enhancement simulations, (b) CO_2 enhancement contributions from different provinces, (c) simulated

anthropogenic CO_2 enhancement proportion for the main sources; Time series (2013 to 2015) of (d) NDVI, (e) SIF, and (f) GPP.

The distance indicates the radius of area centered with NUIST observation site, and the NDVI, SIF, GPP values are averages in

these areas.

1050

1051

1052

1053

1054

1055
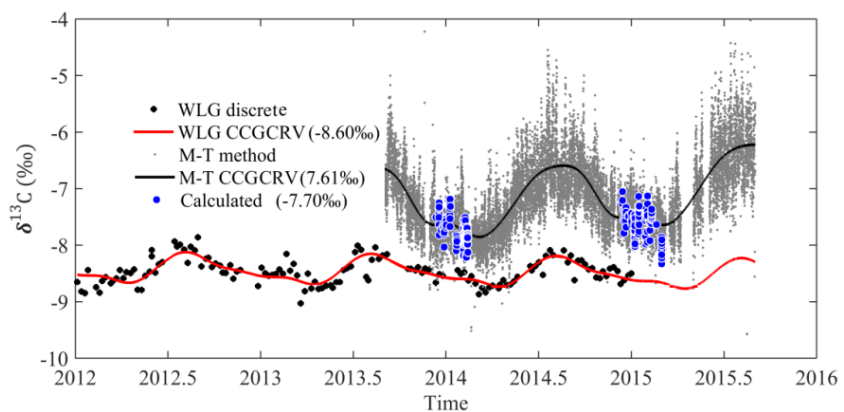
1056

1057   Figure 6. Comparisons among three strategies for calculating the background δ^{13}C-CO$_2$. Strategy 1 (WLG discrete: weekly

1058   discrete observations at WLG site, WLG CCGCRV: derived hourly data with WLG observations and CCGCRV method);

1059   Strategy 2 (Calculated: by choosing clean air in winter); and strategy 3 (M-T method: derived results with observations and M-T

1060   approach, M-T CCGCRV: derived hourly results with M-T approach and CCGCRV method, see details in section 2.2.1).

1061

1062

1063

1064

1065

1066

1067

1068

1069

1070

1071
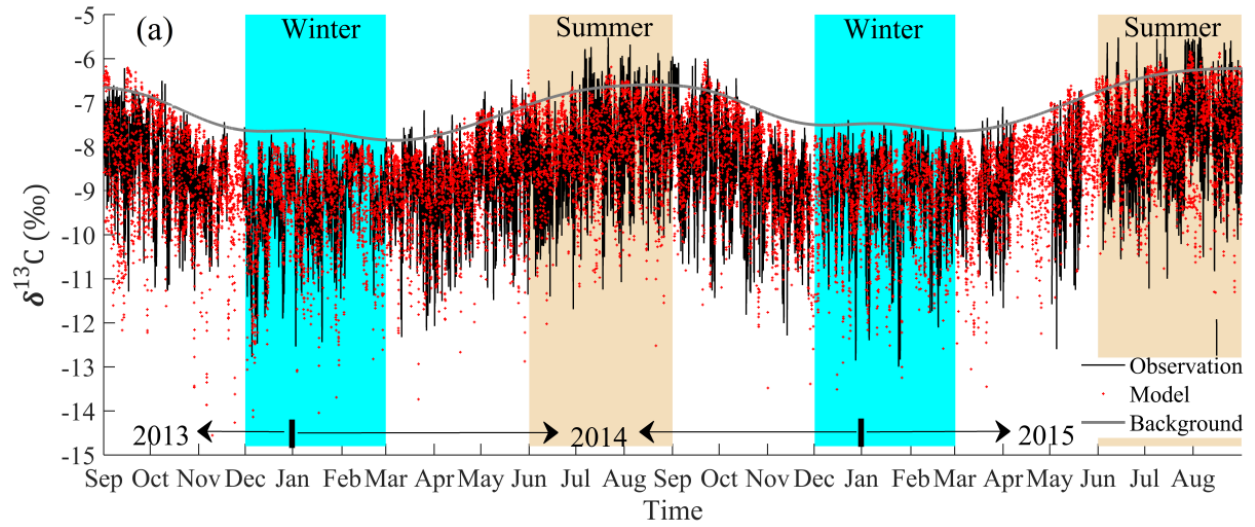
1072

1073
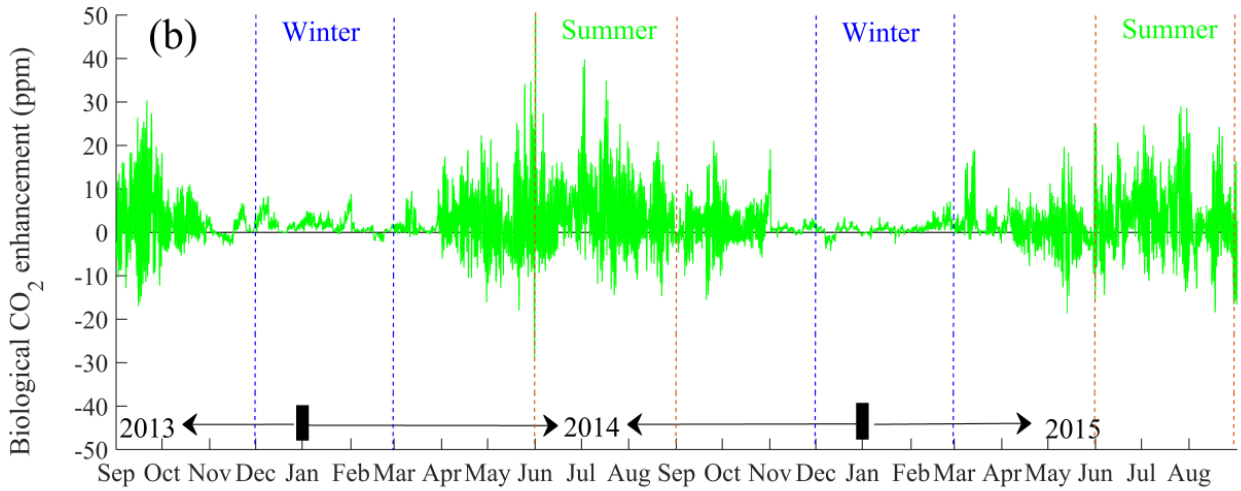
1074

Figure 7. (a) Comparisons of observed and modeled hourly δ^{13}C-CO$_2$ from September 2013 to August 2015, where the grey line represent derived δ^{13}C-CO$_2$ background, and (b) Simulated hourly biological CO$_2$ enhancement. The shade and lines in both subfigures represent the periods for winter and summer, respectively.

1078

1079
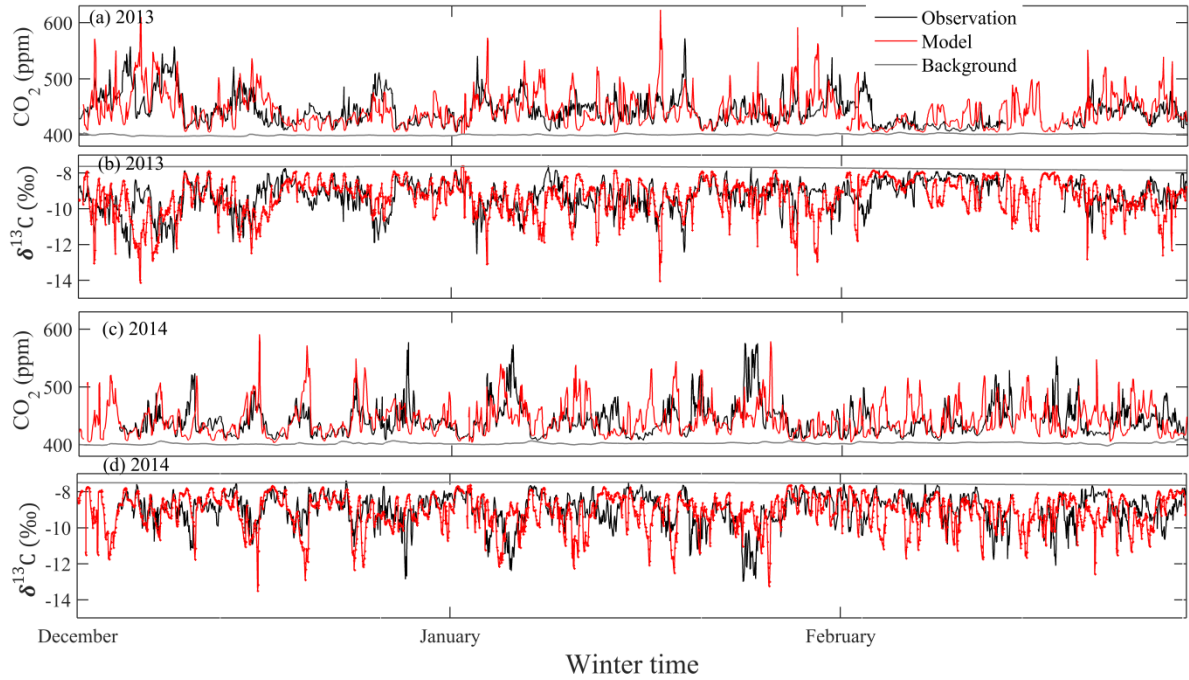
1080
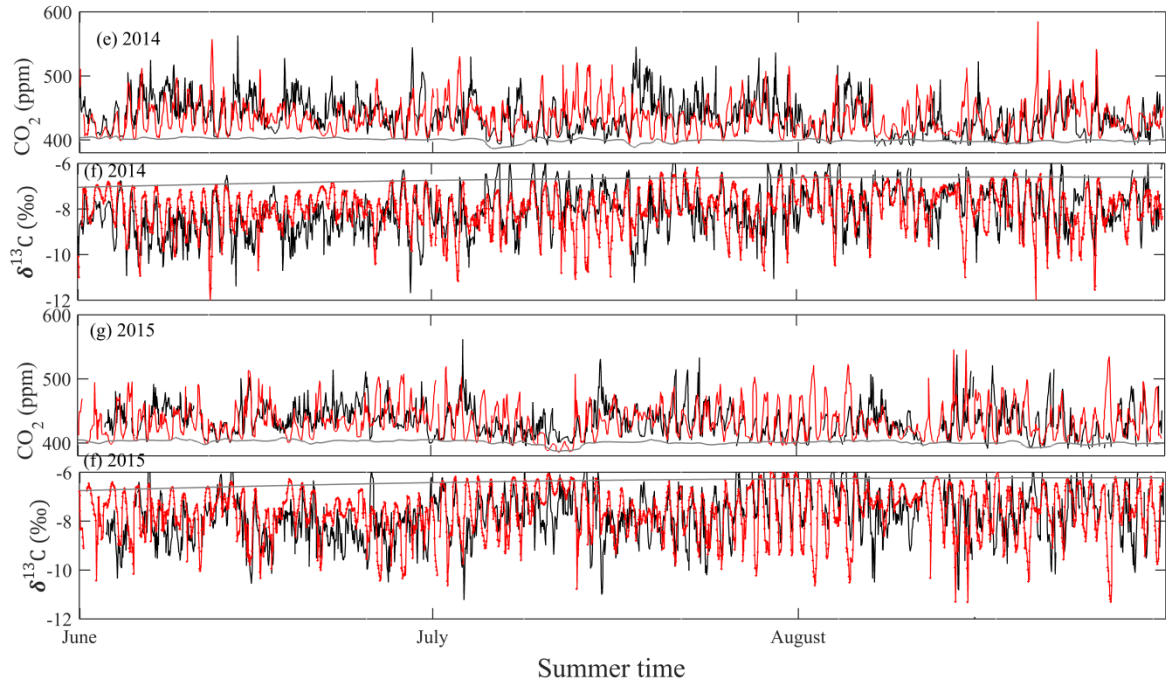
1081

1082

1083   Figure 8. Comparisons of observed and modeled (a) CO_2 mixing ratio and (b) δ^{13}C-CO_2 from December 2013 to February 2014;

1084   (c) CO_2 mixing ratio and (b) δ^{13}C-CO_2 from December 2014 to February 2015; (e) CO_2 mixing ratio and (f) δ^{13}C-CO_2 from

1085   June 2014 to August 2014; (g) CO_2 mixing ratio and (h) δ^{13}C-CO_2 from June 2015 to August 2015.

1086
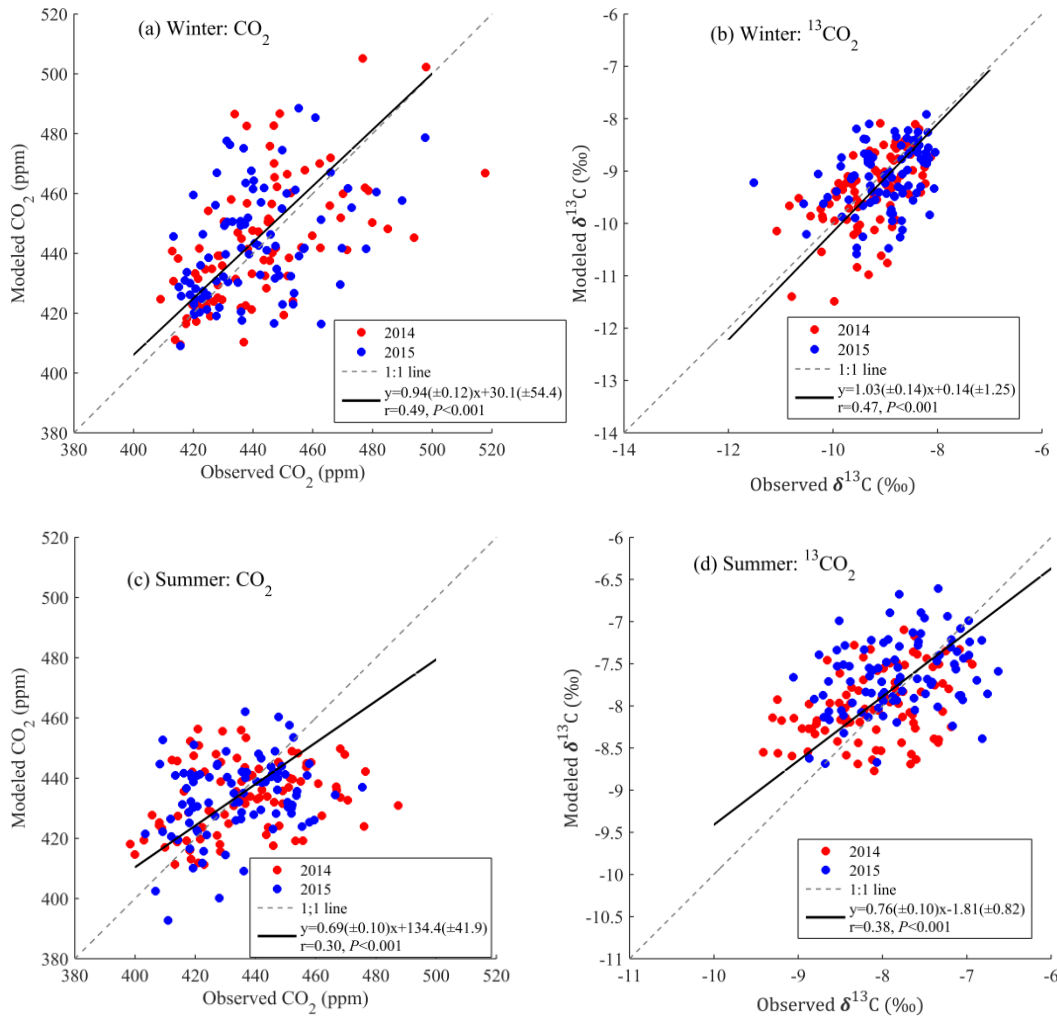
1087

1088

1089   Figure 9. Scatter plots of observed versus modeled (a) winter time CO_2 mixing ratios, (b) winter time δ^{13}C-CO_2, (c) summer time

1090 CO_2, and (d) summer time δ^{13}C-CO_2 for both years, here these dots are daily averages.

1091

1092

1093

1094

1095

1096

1097

1098
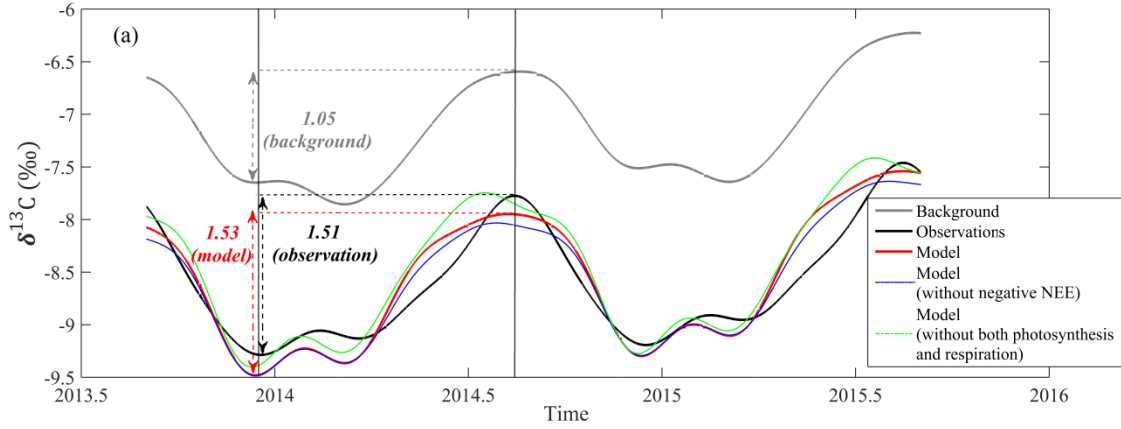
1099
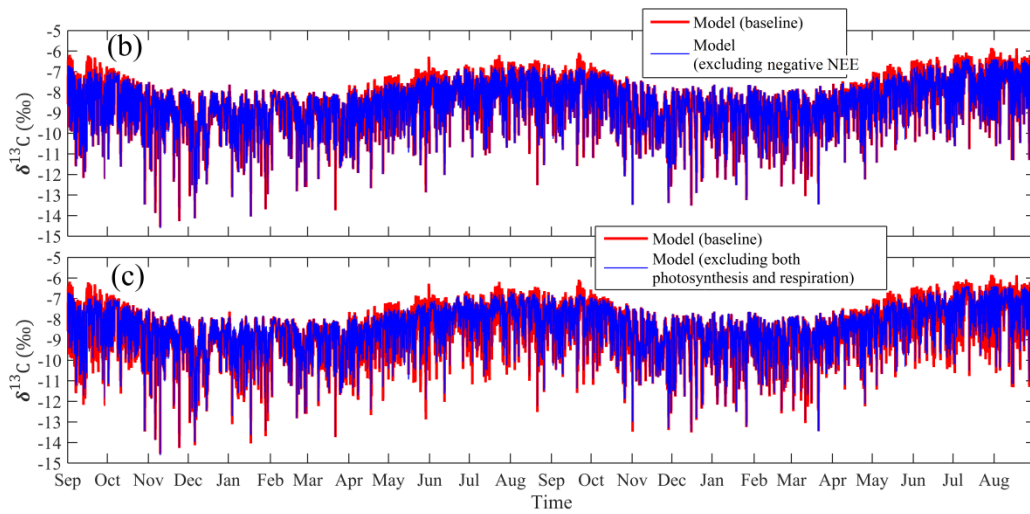
1100

1101 Figure 10. Digital filtering curve fitting (CCGCRV) for background, observations, normal simulations, case 1 (excluding

1102 negative NEE when photosynthesis is stronger than respiration), and case 2 (excluding respiration and photosynthesis) in both

1103 years, (b) δ^{13}C-CO$_2$ comparisons between normal simulations and case 1, and (c) δ^{13}C-CO$_2$ comparisons between normal

1104 simulations and case 2.

1105

1106

1107
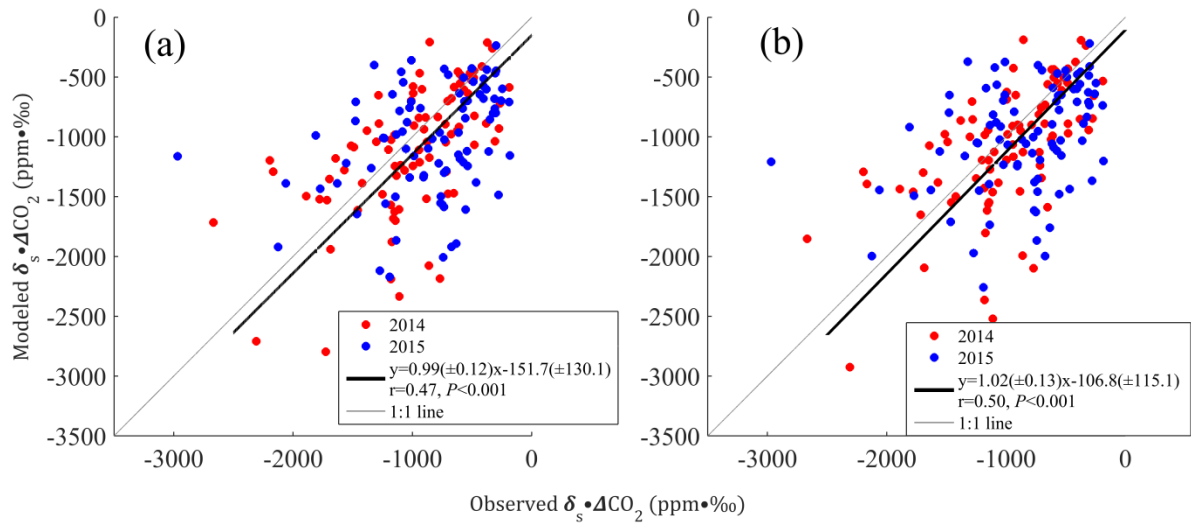
1108

1109   Figure 11. Comparisons of winter time $\delta_s \cdot \Delta CO_2$ using (a) *a priori* and (b) constrained anthropogenic CO_2 emissions.

1110

1111

1112

1113

1114

1115

1116

1117

1118

1119

1120

1121

1122

1123
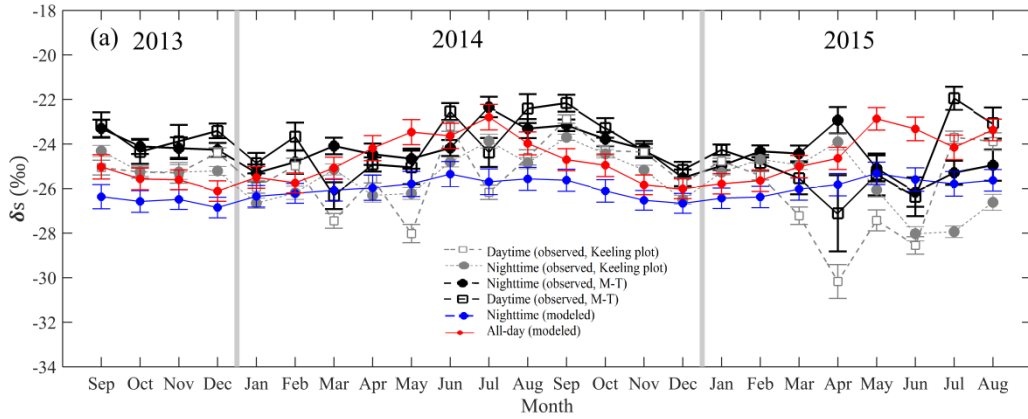
1124
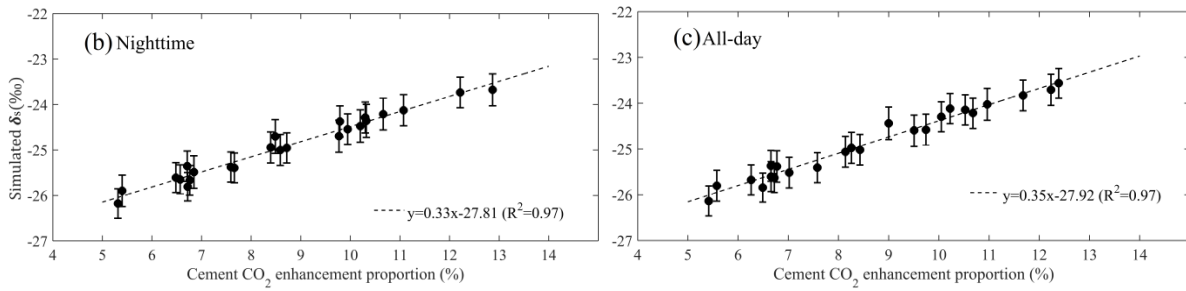
1125

Figure 12. (a) Comparisons between observed and modeled δ_s, (b) relationship between cement CO_2 enhancement proportion and simulated anthropogenic δs for nighttime and (c) all-day.

1128

1129

1130

1131

1132

1133

1134

1135
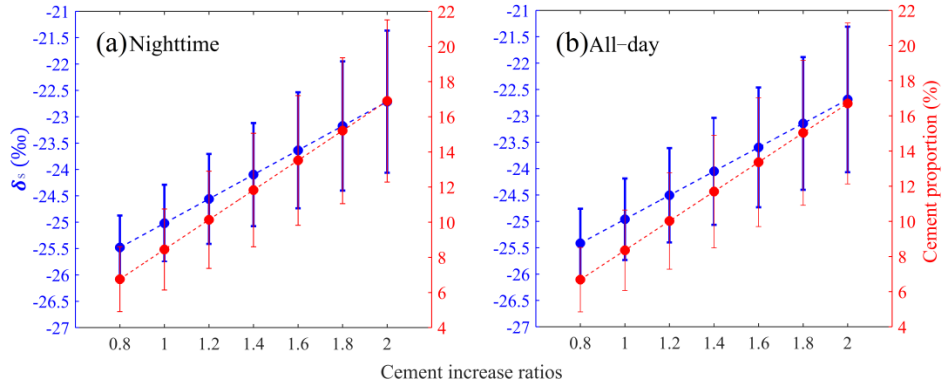
1136
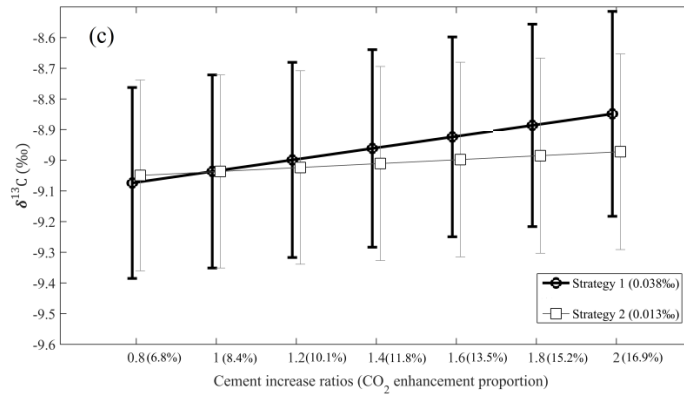
1137

1138
1139
1140
1141
1142
1143
Figure 13. Sensitivity tests showing the influence of cement CO_2 emissions on $\boldsymbol{\delta}_s$ for (a) nighttime, (b) all-day, and (c) the relation between cement CO_2 and $\boldsymbol{\delta}^{13}C$ for simulation strategies 1 (There is no bias in the total anthropogenic CO_2 enhancement such that a proportional increase/decrease in the cement component does not change the relative anthropogenic contributions) and 2 (only the cement enhancement changes). Note that the numbers in brackets indicate changes in $\boldsymbol{\delta}^{13}C$ with cement CO_2 enhancement proportion (the fraction of cement CO_2 enhancement to simulated total CO_2 enhancement) increase by 0.2 times. The x-axis values indicate changing cement enhancement proportions to 0.8 1.2, 1.4, 1.6, 1.8, and 2 times the original values.

1144

1145

1146

1147

1148

1149

1150

1151

1152

1153

1154

1155 Table 1. Comparisons of cement and all anthropogenic CO_2 emissions among different methods, "/" means not available.

Units: $\times 10^{11}$ kg	Year	EDGAR v432	Inversion results	IPCC method
Cement CO_2 emissions	2010	1.45	/	1.14
	2014-2015	1.72	/	1.35
All anthropogenic CO_2 emissions	2010	20.55	/	17.56
	2014-2015	23.53	24.59 ± 2.39	24.38

1156

1157

1158

1159

1160

1161

1162

1163

1164

1165

1166

1167

1168

1169

1170

1171

1172

1173

1174

1175   Table 2. Statistical metrics between observed and modeled CO_2 mixing ratios and $\delta^{13}C$-CO_2 during winter, summer and annual

1176   for 2014 and 2015. Correlation coefficient (R), averages and root mean square error (RMSE) are displayed.

	Years	2014			2015		
	Periods	allyear	Winter	Summer	allyear	Winter	Summer
$\delta^{13}CO_2$ (‰)	R	0.54	0.40	0.47	0.52	0.27	0.39
	RMSE (‰)	1.07	0.94	0.94	1.10	0.92	0.98
	simulation (‰)	-8.68	-9.37	-8.02	-8.45	-9.10	-7.66
	observation (‰)	-8.69	-9.27	-8.09	-8.52	-8.98	-7.83
CO$_2$	R	0.38	0.41	0.34	0.35	0.28	0.31
	RMSE (ppm)	29.44	27.48	25.55	30.22	26.81	24.29
	simulation (ppm)	436.47	441.55	436.67	437.08	442.09	432.37
	observation (ppm)	438.49	442.03	432.25	440.11	440.77	434.71

1177

1178